

1 **A trimeric Rab7 GEF controls NPC1-dependent lysosomal**  
2 **cholesterol export**

3

4 Dick J.H. van den Boomen<sup>1\*</sup>, Agata Sienkiewicz<sup>1</sup>, Ilana Berlin<sup>2</sup>, Marlieke L.M. Jongsma<sup>2</sup>,  
5 Daphne M. van Elstrand<sup>2</sup>, J. Paul Luzio<sup>3</sup>, Jacques J.C. Neefjes<sup>2</sup> and Paul J. Lehner<sup>1\*</sup>

6

7 <sup>1</sup> Cambridge Institute of Therapeutic Immunology & Infectious Disease, University of  
8 Cambridge, Cambridge, United Kingdom.

9 <sup>2</sup> Leiden University Medical Centre, Leiden University, Leiden, the Netherlands.

10 <sup>3</sup> Cambridge Institute for Medical Research, University of Cambridge, Cambridge, United  
11 Kingdom

12 \* Corresponding authors: (DJHB: [djhv2@cam.ac.uk](mailto:djhv2@cam.ac.uk), PJJ: [pjl30@cam.ac.uk](mailto:pjl30@cam.ac.uk), correspondence  
13 address: Cambridge Institute of Therapeutic Immunology & Infectious Disease, University of  
14 Cambridge, Jeffrey Cheah Biomedical Centre, Cambridge Biomedical Campus, Puddicombe  
15 Way, Cambridge CB2 0AW, United Kingdom)

16

17 Running title: A Rab7 GEF controls cholesterol export

18

19 Key words: C18orf8, Mon1, Ccz1, Rab7, GEF, LDL, cholesterol, NPC1, lysosome

20 **Abstract**

21 Cholesterol import in mammalian cells is mediated by the LDL receptor pathway. Here, we  
22 perform a genome-wide CRISPR screen using an endogenous cholesterol reporter and  
23 identify >100 genes involved in LDL-cholesterol import. We characterise C18orf8 as a core  
24 subunit of the mammalian Mon1-Ccz1 guanidine exchange factor (GEF) for Rab7, required  
25 for complex stability and function. *C18orf8*-deficient cells lack Rab7 activation and show  
26 severe defects in late endosome morphology and endosomal LDL trafficking, resulting in  
27 cellular cholesterol deficiency. Unexpectedly, free cholesterol accumulates within swollen  
28 lysosomes, suggesting a critical defect in lysosomal cholesterol export. We find that active  
29 Rab7 interacts with the NPC1 cholesterol transporter and licenses lysosomal cholesterol  
30 export. This process is abolished in *C18orf8*-, *Ccz1*- and *Mon1A/B*-deficient cells and restored  
31 by a constitutively active Rab7. The trimeric Mon1-Ccz1-C18orf8 (MCC) GEF therefore plays  
32 a central role in cellular cholesterol homeostasis coordinating Rab7 activation, endosomal LDL  
33 trafficking and NPC1-dependent lysosomal cholesterol export.

## 34 Introduction

35 Cholesterol is an essential component of all mammalian lipid membranes and disturbances in  
36 its homeostasis associate with a variety of diseases, including Niemann Pick type C, familial  
37 hypercholesterolemia, atherosclerosis and obesity. Cellular cholesterol homeostasis is  
38 transcriptionally regulated by the SREBP2 (sterol response element binding protein 2)  
39 transcription factor. When cholesterol is abundant SREBP2 and its trafficking factor SCAP are  
40 retained in the endoplasmic reticulum (ER), whereas upon sterol depletion they are released  
41 to the Golgi, where SREBP2 is cleaved and traffics to the nucleus to activate the transcription  
42 of genes involved in *de novo* cholesterol biosynthesis (e.g. *HMGCS1*, *HMGCR*, *SQLE*) and  
43 LDL-cholesterol uptake (e.g. *LDLR*, *NPC1/2*)<sup>1</sup>. SREBP2 thus couples cholesterol import and  
44 biosynthesis to cellular cholesterol availability.

45

46 Cholesterol is taken up into mammalian cells in the form of low-density lipoprotein (LDL)  
47 particles, composed predominantly of cholesterol esters (CEs), cholesterol and apolipoprotein  
48 B-100<sup>2</sup>. LDL binds to the cell surface LDL receptor (LDLR) and the LDLR-LDL complex is  
49 internalised via clathrin-mediated endocytosis<sup>3</sup>. In the acidic pH of sorting endosomes, LDL  
50 dissociates from LDLR, which recycles back to the plasma membrane. LDL is itself transported  
51 to a late endosomal / lysosomal (LE/Ly) compartment, where cholesterol is released from CEs  
52 by lysosomal acid lipase (LAL/LIPA). Free cholesterol then binds the Niemann Pick C2 (NPC2)  
53 carrier protein and is transferred to the Niemann Pick C1 (NPC1) transporter for subsequent  
54 export to other organelles<sup>4</sup>.

55

56 NPC1 is a central mediator of lysosomal cholesterol export. Mutations in *NPC1* and *NPC2*  
57 cause Niemann Pick type C, a lethal lysosomal storage disease characterised by lysosomal  
58 cholesterol accumulation in multiple organ systems. *NPC1* encodes a complex polytopic  
59 glycoprotein embedded in the lysosomal membrane<sup>5</sup>. Cholesterol-loaded NPC2 binds the

60 NPC1 middle luminal domain<sup>6, 7</sup> and delivers its cargo to the mobile N-terminal domain<sup>8, 9</sup>,  
61 from where cholesterol is likely transferred to the sterol-sensing domain (SSD). Whether  
62 cholesterol is transported through NPC1 in a channel-like manner or simply inserted into the  
63 luminal membrane leaflet remains unclear<sup>10</sup>. NPC1 is thought to be constitutively active and  
64 no regulators of its activity have been identified. Once transported across the lysosomal  
65 membrane, cholesterol transfer to other organelles is mediated by lipid transfer proteins  
66 (LTPs) at inter-organelle membrane contact sites (MCS)<sup>11</sup>. Although a variety of proteins have  
67 been implicated in MCS formation with LE/Ly<sup>12-15</sup>, the identity of the direct carrier transporting  
68 cholesterol from LE/Ly remains controversial.

69

70 The LE/Ly compartment plays a central role in cellular LDL-cholesterol uptake. LE  
71 homeostasis and substrate trafficking are regulated by the Rab7 GTPase<sup>16</sup>. Rab7 activity is  
72 controlled by its nucleotide status: its activation requires GDP-to-GTP exchange by a  
73 guanidine exchange factor (GEF), whereas GTP hydrolysis induced by GTPase activating  
74 proteins (GAPs) triggers Rab7 inactivation. The active GTP-bound Rab7 associates with LE  
75 membranes and recruits Rab7 effector proteins that mediate a variety of effector functions  
76 including endosome-to-lysosome fusion, endosome motility and recycling<sup>16</sup>. In mammalian  
77 cells Rab7 effectors include the motility factor RILP<sup>17, 18</sup>, the cholesterol binding protein  
78 ORP1L<sup>19, 20</sup>, the VPS34 phosphatidylinositol (PtdIns) 3-kinase regulators Rubicon and  
79 WDR91<sup>21, 22</sup> and the retromer components VPS26 and VPS35<sup>23, 24</sup>.

80

81 Temporal and spatial control of Rab7 activation is of major importance. At least three GAPs –  
82 TBC1D5, TBC1D15 and Armus<sup>24-26</sup> are implicated in Rab7 inactivation, whereas activation of  
83 the yeast Rab7 homologue Ypt7 is mediated by the Mon1-Ccz1 (MC1) complex<sup>27, 28</sup>. MC1 is  
84 recruited to endosomal membranes by the phospholipid PtdIns(3)P<sup>29</sup> and its activation of  
85 Rab7 drives Rab5-to-Rab7 conversion, endosome maturation and fusion with the

86 vacuolar/lysosomal compartment<sup>30-33</sup>. A partial crystal structure of the *C. thermophilum* MC1-  
87 Ypt7 complex suggests a GEF model in which MC1 binding to Ypt7 induces magnesium  
88 expulsion and GDP dissociation from the Ypt7 active site<sup>34</sup>. Mammals have two Mon1  
89 orthologues – Mon1A and Mon1B – and a single Ccz1 orthologue (encoded by two near-  
90 identical genes *Ccz1* and *Ccz1B*). Although mammalian MC1 also likely acts as a Rab7 GEF  
91<sup>35, 36</sup>, its *in vivo* function remains poorly characterised.

92

93 In this study, we perform a genome-wide and sub-genomic CRISPR screen for essential  
94 genes in cholesterol homeostasis using an endogenous SREBP2-dependent cholesterol  
95 reporter. We identify >100 genes mainly involved in the LDL-cholesterol uptake pathway,  
96 including the poorly characterised *C18orf8*. *C18orf8* is a novel core component of the  
97 mammalian MC1 complex, essential for complex stability and function. *C18orf8*-deficient cells  
98 exhibit severe defects in Rab7 activation and LDL trafficking, concomitant with swelling of the  
99 LE/Ly compartment and marked lysosomal cholesterol accumulation. We show that active  
100 Rab7 interacts with the NPC1 cholesterol transporter to license lysosomal cholesterol export  
101 - a pathway which is deficient in *C18orf8*-, *Ccz1*- and *Mon1A/B*-deficient cells and restored by  
102 a constitutively active Rab7 (Q67L). Our findings therefore identify a central role for the trimeric  
103 Mon1-Ccz1-C18orf8 (MCC) GEF in cellular LDL-cholesterol uptake, coordinating Rab7  
104 activation with LDL trafficking and NPC1-dependent lysosomal cholesterol export.

## 105 **Results**

106

### 107 **Generation of an endogenous, SREBP2-dependent, fluorescent cholesterol reporter**

108 To screen for genes that maintain cellular cholesterol homeostasis, we engineered a cell line  
109 expressing an endogenous fluorescent reporter responsive to intracellular cholesterol levels.  
110 HMG-CoA synthase 1 (HMGCS1) catalyses the second step of cholesterol biosynthesis, the  
111 conversion of acetoacetyl-CoA and acetyl-CoA to HMG-CoA. With two sterol-response  
112 elements (SRE) in its promoter, HMGCS1 expression is highly SREBP2 responsive and thus  
113 cholesterol sensitive<sup>37</sup>, rendering it well suited to monitor cellular cholesterol levels (Fig. 1a).  
114 We used CRISPR technology to knock-in the bright fluorescent protein Clover<sup>38</sup> into the  
115 endogenous *HMGCS1* locus yielding an endogenous HMGCS1-Clover fusion protein (Fig. 1b,  
116 Supplementary Fig. 1a). Sterol depletion of the *HMGCS1-Clover* cell line, using mevastatin  
117 and lipoprotein-depleted serum (LPDS), increased basal HMGCS1-Clover expression 9-fold  
118 (Fig. 1d, Supplementary Figs. 1b-c) and revealed the expected cytoplasmic localisation of the  
119 HMGCS1-Clover fusion protein (Fig. 1c). Expression returned to baseline following overnight  
120 sterol repletion (Supplementary Fig. 1d). Sterol-depletion induced HMGCS1-Clover  
121 expression was abolished upon knockout of *SREBP2*, but not its close relative *SREBP1* (Fig.  
122 1d, Supplementary Fig. 1e). *SREBP2*-deficiency also slightly decreased steady-state  
123 HMGCS1-Clover levels (Supplementary Fig. 1f), suggesting low-level SREBP2 activation  
124 under standard growth conditions. Unlike HMG-CoA reductase (HMGCR), HMGCS1  
125 expression is not regulated by sterol-induced degradation (Supplementary Fig. 1g). *HMGCS1-*  
126 *Clover* is therefore a sensitive endogenous, SREBP2-dependent, transcriptional reporter for  
127 intracellular cholesterol levels.

128 **A genome-wide CRISPR screen identifies components essential for cellular cholesterol**  
129 **homeostasis**

130 To identify genes critical to the maintenance of cellular cholesterol levels, we undertook a  
131 genome-wide CRISPR screen using our HMGCS1-Clover reporter as an intracellular  
132 cholesterol sensor (Fig. 1e). CRISPR knockout of these genes is predicted to induce  
133 spontaneous cholesterol depletion, SREBP2 activation and therefore HMGCS1-Clover  
134 upregulation, despite sterol replete (high cholesterol) culture conditions. These cells thus  
135 develop a spontaneous HMGCS1-Clover<sup>high</sup> phenotype. *HMGCS1-Clover* reporter cells were  
136 targeted with a genome-wide CRISPR library containing 10 sgRNAs per gene (total sgRNA  
137 size 220,000) <sup>39</sup> and were sorted in two successive rounds of flow cytometry for the rare  
138 HMGCS1-Clover<sup>high</sup> phenotype (Fig. 1e). This yielded an enriched population with a 60%  
139 HMGCS1-Clover<sup>high</sup> phenotype under sterol replete conditions (Fig. 1f). Next-generation  
140 sequencing of the population revealed sgRNA enrichment for 93 genes (MAGeCK sgRNA  
141 enrichment score  $<10^{-5}$ ) (Fig. 1g, Supplementary Data 1). The results of our HMGCS1-Clover  
142 screen emphasise the central role of LDL-cholesterol uptake and membrane trafficking in  
143 cellular cholesterol homeostasis (Fig 1g, Fig. 2c), with top hits including *LDLR* and *NPC1/2*.

144

145 To validate our genome-wide screening results, we took the top 1000 ranking genes from the  
146 genome-wide screen and created a sub-genomic sgRNA library containing 10 sgRNAs per  
147 gene for the top 1000 genes and 2500 non-targeting sgRNAs (Fig. 2a; total sgRNA size  
148 12,340, Supplementary Data 1). Screening this library as above yielded an enriched  
149 population with a 75% HMGCS1-Clover<sup>high</sup> phenotype (Supplementary Fig. 2a) and sgRNA  
150 enrichment for 65 genes (MAGeCK sgRNA enrichment score  $<10^{-4}$ ) (Supplementary Fig. 2b,  
151 Supplementary Data 1). The majority of these hits (53) overlapped with hits from our genome-  
152 wide screen (Figs. 2a-b, red), confirming reproducibility of our approach. 41 hits were unique  
153 to the genome-wide screen (blue) and 13 were unique to our targeted sub-genomic screening  
154 approach (green). From the identity of these unique hits it is clear that the two screening

155 approaches are complementary as well as overlapping. Whereas the genome-wide screen,  
156 for example, identified multiple components of the COG (COG3/4/7) and vacuolar ATPase  
157 (ATP6AP1/AP2/V0D1/V0E1/V1A/V1B2/V1G1/V1H) complexes, the targeted screen identified  
158 additional subunits (COG5/8, ATP5V1D/V1F) as well as the three V-ATPase assembly factors  
159 CCDC115, TMEM199 and VMA21 (Fig. 2b). Conversely, whereas both screens identified the  
160 AP2  $\mu$ 1 subunit (AP2M1), the genome-wide screen additionally identified the AP2  $\sigma$ 1 subunit  
161 (AP2S1), the AP2 assembly factor AAGAB and accessory factor FCHO2. Our genome-wide  
162 and targeted screening approaches thus provide an extensive overlapping dataset of 106  
163 genes required for cellular cholesterol homeostasis (Fig. 2a-b, Supplementary Data 1).

164

165 Functionally, the hits from our two screens highlight the importance of LDL-cholesterol import  
166 and membrane trafficking in cellular cholesterol homeostasis. They can be grouped in  
167 functional categories (Figs. 1g, Supplementary Fig. 2b) that include: i) protein folding and  
168 glycosylation (yellow, e.g. *HSP90B1*, *GNTAP*, *SLC35A1*); ii) early secretory pathway (pink,  
169 e.g. *ARF1/4*, *COPB1/B2/G2*, *CHP1*, *COG3/4/5/7/8*, *EXOC5/7*); iii) endocytosis (purple, e.g.  
170 *AP2M1/S1*, *AAGAB*, *EHD1*, *FCHO2*, *DNM2*); iv) endosomal trafficking (green, e.g. *RabGEF1*,  
171 *CCZ1/1B*, *Rab5C*, *Rab7A*, V-ATPase  
172 (*ATP6AP1/AP2/V0D1/V0E1/V1A/V1B2/V1D/V1F/V1G/V1H*), ESCRT (*PTPN23*, *HRS*),  
173 CORVET (*VPS8/16/18/TGFBRAP1*), HOPS (*VPS16/18/39/41*), FERARI (*ZFYVE20*, *VPS45*),  
174 PI3K (*BECN*, *UVRAG*, *PIK3R4/C3*), PIKfyve (*FIG4*, *VAC14*)); and v) cholesterol import (blue,  
175 *LDLR*, *NPC1/2*). These categories reflect successive stages in LDL-cholesterol import (Fig.  
176 2c), respectively: i) LDLR folding and glycosylation; ii) trafficking of LDLR to the cell surface;  
177 iii) endocytosis of the LDL-LDLR complex; iv) trafficking of internalised LDL to the LE/Ly  
178 compartment; and v) lysosomal cholesterol release and NPC1-dependent lysosomal  
179 cholesterol export.

180

181 Besides the LDLR pathway, our screen identified components of the SREBP transcriptional  
182 machinery (Fig. 1g, Supplementary Fig. 2b, orange, *INSIG1*, *SREBP1*) and several poorly  
183 characterised gene products (grey/red e.g. *CLU/APOJ*, *EGR3*, *ADAM28*, *FAM160B2*, *STMN4*,  
184 *C18orf8*). To validate our screening results, we confirmed a subset of hits (*LDLR*, *NPC1*,  
185 *AP2 $\mu$ 1*, *ANKFY1*, *VPS16*, *ZFYVE20*, *INSIG1*, *SREBF1*) using individual sgRNAs. All sgRNA-  
186 treated cells showed elevated HMGCS1-Clover expression (Supplementary Fig. 3),  
187 suggesting defective LDL-cholesterol import and/or spontaneous SREBP2 activation.

188

189 Our cholesterol reporter screens therefore provide an extensive overview and unique insight  
190 into both known and unknown factors essential for mammalian LDL-cholesterol import (Fig.  
191 1g, 2c, Supplementary Fig. 2b, Supplementary Data 1), and emphasise the critical role of  
192 endo-/lysosomal trafficking within this process.

193

#### 194 ***C18orf8* is required for endo-lysosomal LDL-cholesterol uptake**

195 A prominent uncharacterised gene in our screens is *C18orf8* (Fig. 1g, Supplementary Fig. 2b,  
196 red), which encodes a 72kDa soluble protein, conserved from animals to plants with no  
197 identifiable yeast orthologue. Structure prediction (Phyre2, HHPred<sup>40, 41</sup>) suggests high  
198 structural similarity to the N-terminus of clathrin heavy chain, with an N-terminal  $\beta$ -propeller  
199 composed of WD40 repeats and a C-terminal  $\alpha$ -helical domain (Supplementary Fig. 5d).  
200 Organelle proteomics have previously identified *C18orf8* as a lysosome<sup>42</sup> and endosome<sup>43</sup>  
201 associated protein.

202

203 To further characterise *C18orf8* function, we generated *C18orf8* knockout clones using two  
204 independent sgRNAs (Fig. 3a). Consistent with our screening results, *C18orf8*-deficient cell  
205 clones showed elevated HMGCS1-Clover expression under sterol-replete culture conditions

206 (Fig. 3b, red line) – implying spontaneous cholesterol depletion – and this phenotype was  
207 reversed upon re-expression of HA-tagged *C18orf8* (*C18orf8*-3HA, green line). Cholesterol  
208 deficiency could result from defective exogenous LDL-cholesterol uptake or defective  
209 endogenous biosynthesis. To differentiate these pathways, we inhibited exogenous uptake by  
210 culturing cells in LPDS or blocked endogenous biosynthesis with mevastatin (Fig. 3c). Wild-  
211 type reporter HeLa cells showed no response to mevastatin alone (Fig. 3c, left panel, red line),  
212 upregulated HMGCS1-Clover in LPDS (green line) and showed maximum reporter induction  
213 in LPDS and mevastatin (blue line). In contrast, *C18orf8*-deficient cells showed elevated  
214 steady-state HMGCS1-Clover expression (Fig. 3c, middle/right panels, black lines), were  
215 unresponsive to LPDS (green lines), but addition of mevastatin alone induced maximum  
216 HMGCS1-Clover induction (red lines) with no further increase in LPDS plus mevastatin (blue  
217 line). These results show that while wild-type HeLa cells rely predominantly on external  
218 cholesterol and switch to endogenous biosynthesis when LDL is unavailable, *C18orf8*-  
219 deficient cells are completely reliant on endogenous cholesterol biosynthesis under all  
220 conditions. This effect is likely explained by a defect in LDL-cholesterol uptake.

221

222 *C18orf8*-deficient cells showed normal LDLR cell surface expression (Supplementary Fig. 4a)  
223 and uptake of fluorescent Dil-LDL (Fig. 3d). However, whereas in wild-type cells Dil-LDL  
224 fluorescence disappeared within 3 hours of pulse-labelling, in *C18orf8*-deficient cells Dil-LDL  
225 accumulated during the 3-hour chase (Fig. 3e), a phenotype rescued upon complementation  
226 with *C18orf8*-3HA. To determine whether this defect is LDL-specific, or derives from a general  
227 endo-lysosomal trafficking defect, we stimulated cells with fluorescent-labelled EGF. Similar  
228 to Dil-LDL, EGF was degraded within 3 hours in wild-type cells, but accumulated during the  
229 3h chase in *C18orf8*-deficient cells (Supplementary Fig. 4b). *C18orf8*-deficient cells thus show  
230 a general defect in endo-lysosomal degradation that affects both LDL and EGF and results in  
231 their reliance on *de novo* cholesterol biosynthesis for cholesterol supply.

232

233 ***C18orf8*-deficient cells are defective in late endosome morphology and early-to-late**  
234 **endosomal trafficking**

235 Consistent with a defect in LDL/EGF degradation, *C18orf8*-deficient cells show a severe  
236 disruption of endosome morphology, in particular of the LE/Ly compartment (Figs. 4a-b,  
237 Supplementary Fig. 4c). Perinuclear Rab7+ LEs (red) were markedly swollen and surrounded  
238 by equally swollen LAMP1+ LE/Lys (green), with EEA1+/Rab5+ EEs (blue) clustered between  
239 Rab7+ LEs in the perinuclear region. By electron microscopy (EM), the swollen LE/Lys  
240 appeared as enlarged multivesicular bodies (MVBs) with a high intraluminal vesicle (ILV)  
241 content and a 3-fold increase in average diameter (Supplementary Fig. 4d). Complementation  
242 of *C18orf8*-deficient cells with *C18orf8*xHA was slow, but after 14 days restored endosome  
243 morphology (Supplementary Fig. 4e) and function (Fig 3e) back to wild-type. This prolonged  
244 recovery likely reflects the severity of the cellular phenotype.

245

246 To assess how this abnormal morphology affects substrate trafficking, we pulse-labelled wild-  
247 type and *C18orf8*-deficient cells with fluorescent-labelled EGF. In both wild-type and *C18orf8*-  
248 deficient cells EGF (red) moved to EEA1+ EE (blue) within ~20min (Fig. 4c). However,  
249 whereas in wild-type cells EGF disappeared from EE at 1-3 hours and was degraded (Fig. 4c,  
250 top panel), in *C18orf8*-deficient cells no degradation occurred and EGF remained in EEA1+  
251 EE for the duration of the 3 hours chase (bottom panel), implying a defect in early-to-late  
252 substrate trafficking. Indeed, inhibiting EGF degradation with Leupeptin, E-64d and Pepstatin,  
253 EGF (red) can be visualised to entry LAMP1+ LE/Ly (green) at 1-3 hours in wild-type (Fig. 4d,  
254 top panel), but not *C18orf8*-deficient cells, in which co-localisation remained minimal  
255 throughout the chase (bottom panel). As seen with EGF, *C18orf8*-deficient cells also  
256 accumulated Dil-LDL in EEA1+ EE for the duration of a 3 hours chase (Fig. 4e) and trafficking  
257 of the fluid phase dye Sulforhodamine 101 (SR101)<sup>44</sup> into lysotracker+ LE/Ly was delayed  
258 (Supplementary Fig. 4f). *C18orf8* therefore plays an essential role in early-to-late and/or late  
259 endosomal trafficking that precedes substrate degradation in lysosomes.

260

261 **C18orf8 is an integral component of the Mon1-Ccz1 complex**

262 To further characterise C18orf8 function, we identified C18orf8-interacting proteins by mass  
263 spectrometry. Pull-down of N- or C-terminal HA-tagged C18orf8 from HeLa cells revealed a  
264 dominant interaction with three proteins – Ccz1, Mon1A and Mon1B – the three components  
265 of the mammalian MC1 complex (Fig. 5a, Supplementary Data 2, PXD021444  
266 [<http://dx.doi.org/10.6019/PXD021444>]). The interaction between overexpressed C18orf8 and  
267 endogenous Ccz1 and Mon1B was readily confirmed by immunoblot (Fig. 5b). To visualise  
268 the interaction between endogenous proteins, we used CRISPR technology to knock-in a  
269 3xMyc-tag into the C18orf8 locus, yielding an endogenous C18orf8-3xMyc fusion  
270 (Supplementary Figs. 5a-b). Pull-down of C18orf8-3xMyc precipitated Ccz1 and Mon1B (Fig.  
271 5c), and conversely immune precipitation of endogenous Mon1B (Fig 5C) or Ccz1  
272 (Supplementary Fig. 5c) revealed the endogenous 3xMyc-tagged C18orf8. C18orf8 is  
273 composed of an N-terminal WD40 and C-terminal  $\alpha$ -helical domain. To identify the MC1-  
274 interaction site in C18orf8, we expressed mScarlet-tagged single domains (Supplementary  
275 Fig. 5d). Immune precipitation revealed an interaction of Ccz1 and Mon1B with the C-terminal  
276 (AA 354-657), but not N-terminal (AA 1-362) domain of C18orf8 (Supplementary Fig. 5e).

277

278 The robust interaction of C18orf8 with all three MC1 components suggests C18orf8 is either  
279 a regulator or integral component of the mammalian MC1 complex. Interestingly, while  
280 *C18orf8*-deficient cells expressed normal levels of Ccz1, they showed a marked reduction in  
281 Mon1B expression (Fig. 5d), which was restored by re-expression of full-length C18orf8 (Fig.  
282 5d), its C-terminal MC1-interaction domain (Supplementary Fig. 5e) or proteasome inhibition  
283 (Supplementary Fig. 5f). Mon1B expression was also decreased in *Ccz1*-deficient cells, while  
284 conversely endogenous C18orf8 expression was reduced in *Ccz1* and *Mon1A/B* double-  
285 deficient cells (Fig. 5e). Mon1B stability is therefore dependent on C18orf8 and Ccz1 and in

286 the absence of either, Mon1B is proteasomally degraded. Similarly, C18orf8 stability depends  
287 on Mon1A/B and Ccz1, whereas Ccz1 remains relatively stable in the absence of both other  
288 components (Fig. 5e). We conclude that mammalian Mon1, Ccz1 and C18orf8 form a stable  
289 trimeric complex, the MCC complex, of which C18orf8 is a core component.

290

291 *C18orf8*, *Ccz1* and *Rab7* are all prominent hits in our screens (Fig. 1g, Supplementary Fig.  
292 2b). To determine whether the function of C18orf8 overlaps with mammalian MC1, we  
293 knocked-out *Ccz1*, *Mon1A*, *Mon1B* and *Rab7* in our *HMGCS1-Clover* reporter line. Similar to  
294 *C18orf8* depletion, loss of *Ccz1* or a combination of *Mon1A* and *Mon1B* - but neither alone -  
295 increased HMGCS1-Clover expression, as did knockout of the *Rab7* GTPase (Fig. 5f). This  
296 phenotype was restored by complementation of knockouts with their respective wild-type  
297 proteins (Supplementary Fig. 5h), with *Mon1A/B*-double-deficient cells rescued by Mon1A or  
298 Mon1B alone. Like *C18orf8*-deficient cells, cells deficient for *Ccz1*- or *Mon1A/B* contained  
299 abnormal, enlarged Rab7+ (red) and LAMP1+ (green) LE/Ly compartments (Fig. 5g). This  
300 phenotypic similarity implies C18orf8 is required for both MCC stability and functionality.  
301 Importantly, although the C18orf8 C-terminal  $\alpha$ -helical domain is necessary and sufficient for  
302 MCC binding and Mon1B stabilization (Supplementary Fig. 5e), it is insufficient for full  
303 complementation of the C18orf8-deficiency phenotype, which required full-length C18orf8  
304 (Supplementary Fig. 5g). C18orf8 is therefore not simply a stabilizing factor but an active  
305 integral component, or subunit, of the mammalian MCC complex.

306

### 307 **The Mon1-Ccz1-C18orf8 complex is responsible for mammalian Rab7 activation**

308 Yeast MC1 acts as an activating GEF for the yeast Rab7 homologue Ypt7<sup>28</sup>. To assess  
309 whether the mammalian MCC complex has a similar function, we expressed HA-tagged wild-  
310 type, dominant-negative (T22N) and constitutively active (Q67L) mutants of Rab7 in C18orf8-  
311 3xMyc knock-in cells and probed their interaction with endogenous MCC components.

312 Consistent with a role in Rab7 activation, C18orf8-3xMyc, Ccz1 and Mon1B preferentially  
313 bound the inactive Rab7-T22N, but not a constitutively active Rab7-Q67L mutant (Fig. 6a).  
314 This interaction is specific to Rab7 and does not occur with other dominant negative GTPases,  
315 including Rab5, Rab9, Rab11 and Arl8B (Supplementary Fig. 6a). Rab7 activation promotes  
316 binding and endosomal recruitment of its effectors RILP and ORP1L<sup>17-20</sup> and effector binding  
317 can be used to assess the activation status of Rab GTPases. In wild-type cells, an interaction  
318 between FLAG-tagged RILP and endogenous Rab7 was readily detected - indicating the  
319 presence of an active GTP-bound Rab7 -, whereas this interaction was completely lost in  
320 *C18orf8*-, *Ccz1*- and *Mon1A/B*-deficient cell lines (Fig. 6b). *MCC*-deficient cells are thus  
321 unable to activate Rab7, suggesting MCC acts as a mammalian Rab7 GEF. Indeed, HA-  
322 tagged RILP (green) was efficiently recruited to LAMP1+ LE/Ly (magenta) in wild-type, but not  
323 in *C18orf8*-deficient cells, where RILP redistributed to the cytoplasm (Fig. 6c). LE recruitment  
324 of the Rab7 effector ORP1L was also strongly reduced (Supplementary Fig. 7a) and consistent  
325 with RILP's function in endosome mobilisation, LE motility was sharply decreased in *C18orf8*-  
326 deficient cells (Supplementary Fig. 7b). *C18orf8*, *Ccz1* and *Mon1A/B* are therefore essential  
327 for Rab7 activation and functional recruitment of the Rab7 effectors RILP and ORP1L in  
328 mammalian cells.

329

### 330 **C18orf8 function can be by-passed by a constitutively active Rab7 or depletion of** 331 **Rab7GAPs**

332 The activation of Rab GTPases by RabGEFs is counteracted by RabGAPs that enhance  
333 intrinsic GTPase activity and revert Rab GTPases back to an inactive state. Our data suggest  
334 that LE defects in *C18orf8*-deficient cells are secondary to defective Rab7 activation. We  
335 therefore asked whether LE function could be rescued by concomitantly blocking one or more  
336 Rab7GAPs; or by the use of a constitutively active Rab7-Q67L mutant that lacks intrinsic  
337 GTPase activity. Knockdown of the Rab7GAPs TBC1D5 and TBC1D15 (Fig. 6d, red line), but  
338 not either alone (green and blue lines), rescued HMGCS1-Clover levels in *C18orf8*-deficient

339 cells back to wild-type (black line) and a similar rescue was obtained by expression of the  
340 constitutively active Rab7-Q67L (Fig. 6e, red line), but not the inactive Rab7-T22N (green  
341 line). Rab7-Q67L also restored the swollen LE/Ly phenotype (Fig. 6f, green) and Dil-LDL  
342 degradation (red) in *C18orf8*-deficient cells. In contrast, the T22N mutant augmented both  
343 phenotypes. Restoration of *C18orf8* function was specific to Rab7 and did not occur with  
344 constitutively active mutants of other endosomal GTPases, including Rab5, Rab9, Rab11 and  
345 Arl8B (Supplementary Fig. 6b). The trimeric Mon1-Ccz1-C18orf8 (MCC) complex therefore  
346 acts as an activating GEF for mammalian Rab7 and its role in late endosomal trafficking and  
347 LDL-cholesterol uptake can be specifically by-passed by a constitutively active Rab7 (Q67L)  
348 or by Rab7GAP depletion.

349

#### 350 **MCC-deficient cells accumulate free cholesterol in their lysosomal compartment.**

351 How does a defect in Rab7 activation result in cellular cholesterol deficiency? *C18orf8*-  
352 deficient cells showed a severe defect in LDL trafficking (Figs. 3e, 4e). We assumed this defect  
353 would impair cholesterol ester (CE) hydrolysis, decrease cholesterol release and, ultimately,  
354 cause cellular cholesterol deficiency. To ascertain the fate of LDL-derived cholesterol, we  
355 stained our cells with Filipin III, a bacterial compound that specifically binds free cholesterol  
356 and differentiates it from CEs in LDL <sup>45</sup>. Remarkably, *C18orf8*-deficient cells did not show a  
357 decrease in Filipin staining, but rather accumulated free cholesterol (green) in their swollen  
358 Rab7+ (blue) and LAMP1+ (red) LE/Ly compartment (Figs. 7a-b). Cholesterol accumulation  
359 resolved upon complementation with *C18orf8*-3xHA (Fig. 7a) and was also observed in *Ccz1*-  
360 and *Mon1A/B*-deficient cells (Fig. 7c). At the ultra-structural level cholesterol accumulation  
361 was confirmed by Theonellamides (TNM) staining <sup>46, 47</sup> which enriched within the enlarged  
362 MVBs of *C18orf8*-deficient cells (Fig. 7d). The accumulation of free cholesterol in LE/Ly of  
363 *MCC*-deficient cells suggests that defective lysosomal cholesterol export, as opposed to LDL  
364 trafficking, is primarily responsible for the cellular cholesterol deficiency in *MCC*-deficient cells.

365 Indeed the *MCC*-deficiency phenotype is strikingly similar to that observed in cells defective  
366 for the NPC1 cholesterol transporter (Fig. 7e).

367

### 368 **Active Rab7 interacts with the NPC1 cholesterol transporter**

369 The NPC1 transporter is critical for lysosomal export of LDL-derived cholesterol and cellular  
370 cholesterol homeostasis (Fig. 1g, Supplementary Figs. 2b, 3) and *NPC1* mutations are the  
371 primary cause of the Niemann Pick type C lysosomal storage disease. *C18orf8*-deficient cells  
372 show normal to elevated levels of NPC1 expression (Supplementary Fig. 8a), with increased  
373 NPC1 expression in *Ccz1*- and *Mon1A/B*-deficient cells (Supplementary Fig. 8b). In wild-type  
374 cells, NPC1 resides predominantly in the LAMP1+ Ly compartment (Supplementary Fig. 8c),  
375 where it co-localises with NPC2 (Supplementary Fig. 8d) and this localisation was unaltered  
376 in *C18orf8*-, *Ccz1*- and *Mon1A/B*-deficient cells (Supplementary Figs. 8c-d). Since NPC1  
377 expression and localisation appeared normal, we used mass spectrometry to identify NPC1  
378 interactions partners. Remarkably, among the most abundant interaction partners identified in  
379 NPC1 immune precipitations is Rab7 itself (Fig. 8a, Supplementary Data 2, PXD021444  
380 [<http://dx.doi.org/10.6019/PXD021444>]). This interaction was confirmed in Rab7:NPC1  
381 immune precipitations, in which NPC1 preferentially bound to the HA-tagged constitutively  
382 active Rab7-Q67L mutant, but not the inactive Rab7-T22N (Fig. 8b), as could be expected for  
383 a functionally important Rab7 interaction. Endogenous Rab7 equally interacted with  
384 endogenous NPC1 (Fig. 8c) and conversely endogenous NPC1 with endogenous Rab7 (Fig.  
385 8d). Consistent with an activation-dependent event, the Rab7-NPC1 interaction seen in wild-  
386 type cells, was lost in *C18orf8*-, *Ccz1*- or *Mon1A/B*-cells that are defective in Rab7 activation  
387 (Fig. 8e). The Rab7-NPC1 interaction is maintained by an inactive NPC1-P692S mutant and  
388 is therefore independent of NPC1's cholesterol export function (Fig. 8f). Indeed Rab7 binding  
389 to NPC1 remained largely unaffected by treatment of cells with LPDS, which decreases, and  
390 the NPC1 inhibitor U18666A, which increases lysosomal cholesterol levels (Fig. 8g).

391

392 **Rab7 activation by the MCC GEF drives NPC1-dependent cholesterol export**

393 Loss of the Rab7-NPC1 interaction in *MCC*-deficient cells correlates with lysosomal  
394 cholesterol accumulation, suggesting Rab7 activation is essential for NPC1-dependent  
395 lysosomal cholesterol export. To test this hypothesis directly and avoid potential caveats  
396 created by LDL trafficking defects, we set up a lysosomal cholesterol export assay analogous  
397 to pulse-chase analysis (Fig. 9a). Cholesterol export was initially blocked using the reversible  
398 NPC1 inhibitor U18666A<sup>48</sup> to induce the accumulation of free cholesterol (green) in CD63+  
399 LE/Ly (magenta) (Fig. 9b; pulse). The inhibitor was then washed out in LDL-free medium  
400 (LPDS) which allowed lysosomal cholesterol efflux in the absence of further LDL-cholesterol  
401 uptake (chase). Cholesterol release from LE/Ly was monitored by Filipin staining (Fig. 9c).  
402 During a 24h chase period, cholesterol (green) was completely exported from CD63+ LE/Ly  
403 (magenta) in wild-type cells, whereas export was abolished in cells deficient for the NPC1  
404 transporter (Figs. 9c-d). Similar to NPC1 deficiency, lysosomal cholesterol export was blocked  
405 in *C18orf8*-, *Ccz1*- and *Mon1A/B*-deficient cells in which Filipin staining remained entirely co-  
406 localised with CD63 during the 24h chase (Figs. 9c-d). To confirm that the cholesterol export  
407 defect in *MCC*-deficient cells depends on defective Rab7 activation, *C18orf8*-deficient cells  
408 were complemented with different Rab7 mutants. While the cholesterol accumulation resolved  
409 upon expression of the constitutively active Rab7-Q67L, no resolution was seen with either  
410 the wild-type or inactive Rab7-T22N (Fig. 9e), confirming Rab7 dependency of the cholesterol  
411 export defect.

412

413 NPC1 function is compromised in type C Niemann Pick (NPC) disease in which lysosomal  
414 cholesterol accumulates in multiple organs. The common NPC1<sup>I1061T</sup> mutation destabilizes the  
415 NPC1 transporter, resulting in its ER retention, and subsequent degradation<sup>49</sup>. However, any  
416 transporter reaching its correct lysosomal location remains functional<sup>50</sup>. We asked whether

417 increased Rab7 activity might improve NPC1 function and promote clearance of lysosomal  
418 cholesterol in mutant NPC1 fibroblasts. Lentiviral overexpression of a GFP-tagged wild-type  
419 Rab7 indeed strongly reduced cholesterol accumulation in NPC1<sup>I1061T/I1061T</sup> patient fibroblasts  
420 (Fig. 9f), suggesting Rab7 activity is limiting for lysosomal cholesterol export in NPC disease.

421

422 Taken together our results show that Rab7 and its trimeric Mon1-Ccz1-C18orf8 (MCC) GEF  
423 control cellular cholesterol homeostasis through coordinated regulation of LDL trafficking and  
424 NPC1-dependent lysosomal cholesterol export, making it a potential therapeutic target in  
425 Niemann Pick disease.

426

## 427 **Discussion**

428 The endocytic uptake of LDL-cholesterol is a major source of cellular cholesterol. Using an  
429 endogenous cholesterol sensor, HMGS1-Clover, in a genome-wide and secondary sub-  
430 genomic CRISPR library screen we identified >100 genes involved in the cellular LDL-  
431 cholesterol uptake pathway. Of these, we characterised C18orf8 as a novel core component  
432 of the Mon1-Ccz1 (MC1) GEF for mammalian Rab7. *C18orf8*-deficient cells are defective for  
433 Rab7 activation, resulting in impaired LDL trafficking and cellular cholesterol depletion. The  
434 unexpected accumulation of free cholesterol in the swollen LE/Ly compartment of *C18orf8*-  
435 deficient cells, suggested an additional critical role for Rab7 in cholesterol export out of  
436 lysosomes. We show that active Rab7 binds the NPC1 cholesterol transporter and licenses  
437 lysosomal cholesterol export. This pathway is defective in *C18orf8*-, *Ccz1*- and *Mon1A/B*-  
438 deficient cells and restored by a constitutively active Rab7 (Q67L). The trimeric Mon1-Ccz1-  
439 C18orf8 (MCC) complex thus plays a central role in cellular LDL-cholesterol uptake,  
440 coordinating Rab7 activation, LDL trafficking and NPC1-dependent lysosomal cholesterol  
441 export.

442

443 Genome-wide CRISPR screens provide a powerful tool to interrogate intracellular pathways.  
444 To avoid artefacts associated with exogenous reporters, we generated an endogenous  
445 SREBP2 knock-in reporter, HMGCS1-Clover, and screened for genes regulating cellular  
446 cholesterol homeostasis. Hits from our primary genome-wide screen were validated in a  
447 secondary targeted screen using a newly generated sub-genomic sgRNA library containing  
448 the top 1000 ranking genes from the primary screen. This approach confirms the  
449 reproducibility of our screening results with 52 out of 65 secondary screening hits present in  
450 our primary screen, while 41 hits were unique to the primary genome-wide screen and 13 hits  
451 unique to the secondary targeted screen (Fig. 2b). As no single genetic screening approach  
452 is sufficient to give a complete picture of a complex cellular pathway, our two screens are  
453 complementary as well as overlapping, with multi-subunit complexes identified across  
454 screens. For example, while our genome-wide screen hits the COG subunits COG3/4/7 and  
455 V-ATPase subunits ATP6AP1/AP2/V0D1/V0E1/V1A/V1B2/V1G1/V1H, our targeted screen  
456 identifies additional subunits (COG5/8, ATP5V1D/V1F) and the V-ATPase assembly factors  
457 CCDC115, TMEM199 and VMA21. Conversely, our targeted screen only identifies the AP2  
458  $\mu$ 1 subunit (AP2M1), whereas our genome-wide screen also identifies the AP2  $\sigma$ 1 subunit  
459 (AP2S1), the assembly factor AAGAB and accessory factor FCHO2.

460

461 The predominant pathway identified by both of our screens is LDL-cholesterol import, as HeLa  
462 cells, like many tissue-culture cells, rely predominantly on cholesterol import rather than *de*  
463 *novo* biosynthesis. The screens identified multiple stages in the LDLR-LDL trafficking pathway  
464 (Fig. 2c), including i) LDLR folding and trafficking to the cell surface; ii) endocytosis of the  
465 LDLR-LDL complex; iii) LDL trafficking to the LE/Ly compartment; and iv) NPC1 dependent  
466 cholesterol export from LE/Ly. Functional complexes identified include COG, Exocyst, AP2,  
467 V-ATPase, PI3K, PIKfyve, CORVET, HOPS, FERARI and GARP; poorly characterised genes  
468 include the chaperone Clusterin (also known as Apolipoprotein J) and the metalloprotease

469 ADAM28. Our genome-wide and targeted CRISPR screens thus provide an extensive  
470 overlapping dataset of 106 genes required for LDL-cholesterol import, and identify novel  
471 candidate genes in this pathway.

472

473 Spatial and temporal control of Rab7 activation is critical to coordinate substrate trafficking  
474 and degradation in LE/Ly<sup>16</sup>. In yeast the dimeric Mon1-Ccz1 (MC1) GEF activates the Rab7  
475 homologue Ypt7<sup>27, 28</sup> and a similar function has been suggested for mammalian MC1<sup>35, 36</sup>.  
476 We find that a stable trimeric complex of Mon1A/B, Ccz1 and C18orf8 (MCC) is required for  
477 Rab7 activation in mammalian cells, as defined by effector recruitment. *C18orf8*, *Mon1* and  
478 *Ccz1* are conserved from animals to plants, but a *C18orf8* orthologue is missing from  
479 laboratory yeast and most other fungi, either due to divergence of the endocytic machinery or  
480 because C18orf8 function is incorporated into other components.

481

482 Rab7 is a key regulator of LE homeostasis and *C18orf8*-, *Ccz1*- and *Mon1A/B*-deficient cells  
483 show a broad range of LE defects including LE morphology, endosomal substrate trafficking,  
484 lysosomal degradation and cholesterol export. Consistent with a previous Rab7 depletion  
485 study<sup>51</sup>, *C18orf8*-deficient cells accumulate enlarged MVBs; and consistent with current Rab5-  
486 to-Rab7 conversion models<sup>32</sup> we observe a delay in early-to-late endosomal trafficking.  
487 Whereas LDL trafficking was previously suggested to involve only Mon1B<sup>52</sup>, we find that only  
488 the combined depletion of Mon1A/B causes cholesterol deficiency, suggesting redundancy of  
489 Mon1 homologues.

490

491 Besides LE trafficking, Rab7 is an important factor in autophagy<sup>53</sup>. During preparation of this  
492 manuscript, a role for C18orf8 was reported as a regulator of autophagic flux<sup>54</sup>. Like us, this  
493 group reports a robust interaction between C18orf8 and mammalian MC1. Without direct  
494 evidence of Rab7 activation, C18orf8 is however postulated to be a MC1 regulator. We find

495 C18orf8 is not a regulator, but a core subunit of the trimeric mammalian MCC complex, which  
496 acts as a Rab7 GEF. Stability of the three core components is interlinked, with Mon1B stability  
497 dependent on C18orf8 and Ccz1, and C18orf8 stability dependent on Ccz1 and Mon1B. Ccz1  
498 appears relatively stable in the absence of both other components and may therefore form a  
499 scaffold for Mon1A/B and C18orf8 assembly. The intricate relationship between C18orf8 and  
500 Mon1A/B is intriguing as Phyre2 prediction suggests C18orf8 adopts a clathrin-like fold, while  
501 Mon1A/B shows structural similarity to the AP2 $\mu$  subunit<sup>55</sup>. Whether this structural similarity  
502 has functional consequences, remains to be established.

503

504 The structural interdependence of the MCC subunits complicates *in vivo* studies to assess the  
505 direct role of C18orf8 in mammalian MCC. Yeast Ccz1p and Mon1p are necessary and  
506 sufficient for Ypt7 binding and GDP-to-GTP exchange, with most of the MC1-Ypt7 binding  
507 interface mediated by Mon1p<sup>28, 34</sup>. Residues critical for Ypt7 binding are conserved in  
508 mammalian MC1 and a dimeric complex of mammalian Mon1A and Ccz1 was shown to have  
509 limited *in vitro* Rab7 GEF activity<sup>36</sup>. While this complex might have retained residual C18orf8  
510 due to its isolation from mammalian cells, future studies will address whether C18orf8  
511 contributes towards *in vitro* MC1 GEF activity.

512

513 *In vivo*, C18orf8 function goes beyond being a scaffold for MCC stabilisation. The C18orf8 C-  
514 terminal  $\alpha$ -helical domain is sufficient to bind MC1 and stabilize Mon1B, but insufficient to fully  
515 restore MCC function (Supplementary Figs. 5e, 5g). The C18orf8 N-terminus thus has an  
516 independent function and may bind other trafficking components and/or membrane lipids. The  
517 timing of Rab7 activation is strictly regulated to coordinate Rab5-to-Rab7 conversion and likely  
518 requires control of MCC by upstream components<sup>32</sup>. Membrane association allosterically  
519 activates yeast MC1 and increases its GEF activity ~1600-fold<sup>29</sup>. Like yeast Mon1p and Ccz1p,  
520 mammalian Mon1A binds PtdIns3P and PtdSer<sup>27</sup>, while positively charged residues in the N-

521 terminal  $\beta$ -propeller of C18orf8 are well positioned to bind negatively charged phospholipids.  
522 In analogy to AP2<sup>56</sup>, PtdIns binding might open the MCC complex towards Rab7 binding, thus  
523 allosterically activating MCC upon membrane association.

524

525 Cholesterol is hydrolysed from CEs in a LE/Ly compartment, and NPC1 is essential for its  
526 subsequent export to the ER, mitochondria and plasma membrane. Increased expression of  
527 our SREBP2 reporter indicates *C18orf8*-, *Ccz1*- and *Mon1A/B*-deficient cells are starved of  
528 ER cholesterol, yet paradoxically they accumulate free cholesterol in a swollen LE/Ly  
529 compartment. This suggested a novel role for Rab7 in lysosomal cholesterol export. We find  
530 an active Rab7 binds the lysosomal cholesterol transporter NPC1 and licenses its export of  
531 LDL-derived cholesterol from LE/Ly. The inability of MCC-deficient cells to activate Rab7,  
532 results in a Niemann-Pick-like phenotype, even though NPC1/NPC2 expression and  
533 localisation are intact. Rab7 therefore functions as a novel regulator of NPC1 and its export of  
534 lysosomal cholesterol.

535

536 The mechanism by which Rab7 controls NPC1-dependent lysosomal cholesterol export  
537 remains at present unclear. There is however at least three ways in which Rab7 might regulate  
538 this key process: (i) Rab7 may directly activate the NPC1 transporter, thus licensing lysosomal  
539 cholesterol export (Fig. 10a); (ii) Rab7 might assemble a lipid transfer hub down-stream of  
540 NPC1 to allow inter-organelle cholesterol transfer at membrane contact sites (MCS) (Fig. 10b);  
541 or (iii) Rab7 may act by a combination of both.

542

543 The activity of many transporters is tightly regulated as exemplified by the lysosomal calcium  
544 channel TRPML1, which is activated at LE/Ly by PtdIns(3,5)P<sub>2</sub><sup>57</sup>. Even so, the NPC1  
545 transporter is believed to be constitutively active and to date no NPC1 regulators have been  
546 identified. So why would Rab7 regulate NPC1 activity? Inappropriate cholesterol export by a  
547 nascent NPC1 could harm the composition and functionality of non-lysosomal compartments.

548 To prevent cholesterol export outside LE/Ly, the cholesterol hand-off between NPC2 and  
549 NPC1 relies on an acidic lysosomal pH<sup>7</sup>. Rab7's activation of NPC1-dependent cholesterol  
550 export could further restrict cholesterol transfer to the appropriate LE/Ly compartment (Fig.  
551 10a). The Rab7-NPC1 interaction is independent of lysosomal cholesterol content. Even so,  
552 variations in Rab7 activity might tune lysosomal cholesterol export to cellular or organelle-  
553 specific conditions, such as MCS formation or organelle division. Future studies will aim to  
554 identify the cytoplasmic Rab7 binding site on NPC1 and its putative function in regulating  
555 NPC1 activity.

556

557 Besides NPC1 activation, Rab7 might control lysosomal cholesterol export through the  
558 formation of inter-organelle membrane contact sites (MCS) and/or the recruitment of lipid  
559 transfer proteins (LTPs) down-stream of NPC1 (Fig. 10b). At least three Rab7 effectors -  
560 ORP1L, Protrudin (ZFYVE27) and PDZD8 – have been involved in ER-to-LE MCS formation<sup>19</sup>,  
561 <sup>20, 58, 59</sup> and Rab7 itself has been implicated in ER-to-mitochondria MCS formation<sup>60</sup>. MCS are  
562 of key importance for rapid inter-organelle lipid exchange, yet whether Rab7-mediated MCS  
563 are involved in cholesterol transfer remains controversial. The Rab7 effector ORP1L was  
564 reported to act as a LTP linking the ER and LE/Ly and transporting cholesterol towards the  
565 ER in a PtdIns(4,5)P<sub>2</sub> / PtdIns(3,4)P<sub>2</sub>-dependent manner<sup>12, 61</sup>. ORP1L depletion however  
566 causes only minor steady-state changes in lysosomal cholesterol, as does depletion of other  
567 LTPs and tethering proteins such as STARD3, ORP5 and SYT7<sup>13, 14, 62</sup>. By contrast, *C18orf8*-  
568 , *Ccz1*- and *Mon1A/B*-deficient cells are entirely defective in lysosomal cholesterol export and  
569 fully phenocopy an NPC1-deficiency phenotype (Figs. 7d, 9c-d). This places Rab7 firmly at  
570 the centre of lysosomal cholesterol export and suggests the LTP(s) involved might be Rab7  
571 effectors. Future studies will aim to identify the full set of (redundant) Rab7-effectors and LTPs  
572 involved in lysosomal cholesterol export.

573

574 LDL-cholesterol uptake is a highly efficient process, with each LDLR molecule estimated to  
575 endocytose one LDL particle containing ~1600 CE/cholesterol molecules every 10min<sup>3</sup>.

576 Down-stream LDL processing must be tightly coordinated to prevent a backlog in the endocytic  
577 pathway. CE hydrolysis likely commences *en route* to NPC1+ Ly to allow the large LDL particle  
578 to unpack; whereas the arrival and export of cholesterol in Ly must be linked to the formation  
579 and transport capacity of MCS. As a central regulator of LE homeostasis, Rab7 is well suited  
580 to coordinate these processes. Indeed, *MCC*-deficient cells show defects in LDL trafficking  
581 and lysosomal cholesterol export, indicating both are linked to the Rab7 nucleotide cycle. We  
582 propose that Rab7 and its MCC GEF are central regulators of cellular LDL-cholesterol uptake,  
583 coordinating LDL trafficking, NPC1-dependent lysosomal cholesterol export and lipid transfer  
584 at MCS. Besides cholesterol, the Rab7 lipid transfer hub might mediate lysosomal egress of  
585 other lipids, with VPS13A/C prominent Rab7 effectors<sup>63, 64</sup>.

586

587 Mutations in NPC1 and NPC2 cause the lethal Niemann Pick type C (NPC) lysosomal storage  
588 disease. Disease-associated mutations commonly destabilize NPC1, leading to its ER  
589 retention and proteasome- or lysosome-mediated degradation<sup>49, 65</sup>. The most prevalent NPC1  
590 mutation, I1061T, destabilizes NPC1, yet the mutant protein retains its cholesterol export  
591 function and the disease phenotype can be restored by overexpression of the mutant NPC1<sup>50</sup>.  
592 Confirming earlier observations<sup>66</sup>, we show lentiviral overexpression of a GFP-tagged wild-  
593 type Rab7 reduces cholesterol accumulation in NPC1<sup>I10161T/I1061T</sup> patient-derived primary  
594 fibroblasts (Fig. 9f). Whereas this rescue was previously ascribed to enhanced vesicular  
595 trafficking, we suggest that Rab7 overexpression directly enhances NPC1-dependent  
596 lysosomal cholesterol export. This effect depends on an active Rab7 and is not observed with  
597 the inactive Rab7-T22N, whereas the hyperactive Rab7-Q67L shows an intermediate  
598 phenotype (Supplementary Fig. 9). A modest increase in Rab7 activity therefore increases  
599 lysosomal cholesterol clearance in NPC1-mutant cells while optimal clearance requires both  
600 Rab7 activation and inactivation in a time- and location-dependent manner.

601

602 In summary, we have identified a novel function for the Rab7 GTPase and its trimeric Mon1-  
603 Ccz1-C18orf8 (MCC) GEF in the coordination of late endosomal LDL trafficking and NPC1-

604 dependent lysosomal cholesterol export. Future studies will aim to further characterise the  
605 mechanism behind Rab7 function in lysosomal cholesterol export and explore its therapeutic  
606 potential in Niemann Pick disease.

607 **Methods**

608

609 **Materials**

610 Details of all plasmids, shRNA and sgRNA constructs, gene fragments, primers and antibodies  
611 used in this study are indicated in the Supplementary Methods. Primers were purchased from  
612 Sigma-Aldrich, gene fragments from Integrated DNA Technologies (IDT).

613

614 **Cell lines**

615 HeLa and 293T cells were maintained respectively in RPMI-1640 and IMDM (Sigma-Aldrich)  
616 supplemented with 10% foetal calf serum (FCS). For sterol depletion, cells were washed in  
617 PBS and incubated overnight in RPMI supplement with 5% lipoprotein-depleted serum (LPDS,  
618 Biosera), 10 $\mu$ M mevastatin (Sigma-Aldrich) and 50 $\mu$ M mevalonate (Sigma-Aldrich).  
619 NPC1<sup>I1061I/I1061T</sup> patient-derived primary fibroblasts (GM18453) and healthy controls  
620 (GM08399) were obtained from Coriell Institute for Medical Research (New Jersey, USA) and  
621 grown in MEM with Earl's salt (Sigma-Aldrich) supplemented with 15% FCS and non-essential  
622 amino acids (Gibco).

623

624 CRISPR knock-out lines were created by transient transfection of HeLa cells using TransIT  
625 HeLa Monster (Mirus). Transfected cells were selected on puromycin 24-72h post-transfection  
626 and single-cell cloned >7 days post-transfection. Knock-out clones were characterised by flow  
627 cytometry and Western blotting.

628

629 Stable protein overexpression was achieved using lentiviral transduction. Briefly, 293T cells  
630 were co-transfected in a 1:1 ratio with a lentiviral expression vector (pHRSIN/pHRSiren/pKLV)  
631 and the packaging vectors pMD.G and pCMVR8.91 using TransIT-293 (Mirus). Supernatant  
632 was harvested at 48h post-transfection and transferred onto target cells. Cells were spun  
633 60min at 700g to enhance infectivity and incubated with virus overnight. Transduced cells

634 were selected for stable transgene expression with appropriate antibiotics from 48h post-  
635 transduction.

636

### 637 **CRISPR knock-in of C-terminal tags**

638 HeLa cells were transiently transfected with sgRNA, CAS9 and pDonor vector using TransIT  
639 HeLa Monster (Mirus). To create a C18orf8-3xMyc knock-in a single donor vector (pDonor  
640 C18orf8-3xMyc Hygro, Supplementary Fig. 5a) was used, whereas for HMGCS1-Clover  
641 knock-in a combination of three donor plasmids (pDonor HMGCS1-Clover Puro, Hygro, Blast,  
642 Supplementary Fig. 1a) was used to select for multiple-allele integration. Transfected cells  
643 were transiently selected for sgRNA expression using puromycin at 24-72h post-transfection,  
644 followed by selection of the knock-in cassette using hygromycin or a combination of  
645 puromycin, hygromycin and blasticidin at 7 days post-transfection. Selected cells were  
646 transiently transfected with Cre recombinase to remove resistance cassettes and single-cell  
647 cloned. Single cell clones were characterised using flow cytometry and Western blotting.

648

### 649 **Cloning of the top 1000 sub-genomic sgRNA library**

650 The top 1000 sub-genomic sgRNA library was cloned as detailed previously<sup>67, 68</sup>. sgRNA  
651 sequences for the top 1000 genes of the genome-wide CRISPR screen were retrieved from  
652 the Bassik genome-wide CRISPR library (10 sgRNAs / gene, Supplementary Data 1)<sup>39</sup>.  
653 Duplicate sgRNAs and sgRNAs with internal BsmBI sites were replaced with sgRNAs derived  
654 from the genome-wide Sabatini library<sup>69</sup> or designed *de novo* using the Broad Institute sgRNA  
655 designer (<https://portals.broadinstitute.org/gpp/public/analysis-tools/sgrna-design>). Targeting  
656 sgRNAs (total 9936) were appended with the overhangs 5'-  
657 AGGCACTTGCTCGTACGACGCGTCTCACACCG-sgRNA(17-20nt)-  
658 GTTTCGAGACGATGTGGGCCCGGCACCTTAA-3' and 2500 non-targeting sgRNAs  
659 (derived from the genome-wide Bassik library) were added with the overhangs 5'-  
660 GTGTAACCCGTAGGGCACCTCGTCTCACACCG-sgRNA(17-20nt)-  
661 GTTTCGAGACGGTCGAGAGCAGTCCTTCGAC-3'. The pooled oligo library (total 12,346

662 sgRNAs, Supplementary Data 1) was synthesised by GenScript (Netherlands). Targeting and  
663 non-targeting oligos were amplified separately using Q5 hot-start polymerase (NEB) and  
664 primers indicated in the Supplementary Materials. PCR products were digested with BsmBI  
665 (Thermo-Fisher), ligated in a BsmBI-digest modified pKLV.U6 pGK Puro-2A-BFP vector and  
666 transformed at >30-fold coverage in ElectroMax Stbl4 competent cells. Plasmid DNA was  
667 prepped using a Qiagen Plasmid Maxi Kit.

668

### 669 **Genome-wide and targeted sub-genomic CRISPR screening**

670 HeLa HMGCS1-Clover cells were stably transduced with Cas9. CRISPR sgRNA library  
671 lentivirus was produced as indicated above and titrated on HeLa HMGCS1-Clover Cas9 cells.  
672 For genome-wide CRISPR screening,  $1 \times 10^8$  HeLa HMGCS1-Clover Cas9 cells were  
673 transduced at 30% infectivity (>100-fold coverage) with the genome-wide Bassik library<sup>39</sup>,  
674 puromycin selected, sorted at day 9 ( $7.4 \times 10^7$  cells at 0.56%) and again at day 18 ( $1.9 \times 10^7$   
675 cells at 3.1%) for a HMGCS1-Clover<sup>high</sup> phenotype. Sorted cells were grown for another 5  
676 days, harvested ( $5 \times 10^6$  cells) and genomic DNA was extracted using a Gentra Puregene Core  
677 kit A (Qiagen).

678

679 For targeted sub-genomic CRISPR screening  $2.4 \times 10^7$  HeLa HMGCS1-Clover CAS9 cells  
680 were transduced at 28% infectivity (>500-fold coverage) with the top 1000 sgRNA library,  
681 puromycin selected, sorted at day 8 ( $5.2 \times 10^7$  cells at 1.1%) and again at day 12 ( $1.5 \times 10^7$  cells  
682 at 6.7%) for a HMGCS1-Clover<sup>high</sup> phenotype and genomic DNA was extracted from sorted  
683 cells ( $5 \times 10^5$ ) and an age-matched library sample ( $1 \times 10^7$  cells) at day 12.

684

685 Integrated sgRNA was amplified via two rounds of PCR using primers as indicated in  
686 Supplementary Methods, starting with 400µg and 100µg of gDNA respectively for the library  
687 and sorted sample of the genome-wide CRISPR screen and 200µg and 14µg gDNA for the  
688 library and sorted sample of the sub-genomic CRISPR screen. PCR products were purified  
689 using AMPure XP beads (Agencourt), quantified on a DNA-1000 chip (Agilent) and sequenced

690 on a Miniseq sequencer (Illumina) running MiniSeq Control Software v1.1.8 (Illumina). Reads  
691 were aligned to library sequences using Bowtie<sup>70</sup>, allowing read alignment to a maximum of 2  
692 sgRNA and 1 mismatch. sgRNA abundance in the sorted sample was compared against a  
693 library sample of similar age (genome-wide screen) or a screen-internal library sample  
694 (targeted screen) and sgRNA enrichment was computed using the MAGeCK algorithm under  
695 default settings<sup>71</sup>. Enrichment and de-enrichment of individual targeting and non-targeting  
696 sgRNAs is plotted in Supplementary Fig. 10. Hits with a MAGeCK score  $<10^{-5}$  (genome-wide  
697 screen) or  $<10^{-4}$  (targeted screen) were manually annotated into functional pathways  
698 (cholesterol import, endocytosis, endosomal trafficking, ER/Golgi trafficking, protein  
699 folding/glycosylation, SREBP pathway) (Fig. 2c). Full datasets, including read counts,  
700 MAGeCK analysis and selected hits, are available in Supplementary Data 1.

701

## 702 **Immunoblotting and Immunoprecipitation**

703 For immunoblotting, cells were lysed for 30 min on ice in 1% IGEPAL (Sigma-Aldrich) or 1%  
704 Digitonin (Merck) in TBS pH 7.4 with Roche complete protease inhibitor or for 30 min at RT in  
705 2% SDS in 50mM Tris pH7.4 in the presence of Benzonase (Sigma-Aldrich). Post-nuclear  
706 supernatants were heated 15 min at 50°C in SDS sample buffer, separated by SDS-PAGE  
707 and transferred to PVDF membranes (Millipore). Membranes were probed with the indicated  
708 antibodies and reactive bands visualised with ECL, Supersignal West Pico or West Dura  
709 (Thermo Scientific).

710

711 For immunoprecipitations, cells were lysed for 30 min on ice in 1% Digitonin, 1% IGEPAL or  
712 0.5% IGEPAL in TBS pH 7.4 with Roche protease inhibitor. Samples were precleared with  
713 protein A/IgG-Sepharose and incubated with primary antibody and protein A/protein G-  
714 Sepharose or antibody conjugated agarose for at least 2 hrs at 4°C. After 5 washes in 0.2%  
715 detergent, proteins were eluted in 2% SDS, 50mM Tris pH7.4, separated by SDS-PAGE and  
716 immunoblotted as described. For RILP/NPC1/Rab7 immune precipitations, lysis buffers were  
717 supplemented with 10mM MgCl<sub>2</sub> and 1mM EDTA.

718

719 **Metabolic labelling and pulse-chase**

720 Cells were sterol-depleted overnight, starved for 30 min at 37°C in methionine-free, cysteine-  
721 free RPMI containing 5% dialysed LPDS, labelled with [<sup>35</sup>S]methionine/[<sup>35</sup>S]cysteine)  
722 (Amersham) for 10 min and then chased in RPMI with 10% FCS supplemented with 2 µg/ml  
723 25-hydroxy-cholesterol and 20 µg/ml cholesterol. Samples taken at the indicated time-points  
724 were lysed in 1% Digitonin/TBS as above. Immunoprecipitations were performed as above,  
725 washed with 1% Tx-100/TBS, eluted and samples separated by SDS-PAGE and processed  
726 for autoradiography with a Cyclone scanner (Perkin-Elmer).

727

728 **Flow cytometry**

729 Cells were washed in PBS, detached by trypsinising for 5 min, pelleted and where necessary  
730 antibody stained for 30min on ice. After washing in ice-cold PBS, cells were analysed on a  
731 FACS Calibur or FACS Fortessa (BD Biosciences) using BD CellQuant v5.2 and FACSDiva  
732 v8.0.1 software respectively, and analysed in FlowJo v10.6.1(LCC).

733

734 **Immune fluorescence**

735 Cells were grown on 10mm coverslips, fixed for 15 min in 4% formaldehyde (Polysciences),  
736 washed 3 times with PBS and incubated 10 min with 15mM Glycine. Cells were permeabilised  
737 for 1 hour with 0.05% saponin, 5% goat serum in PBS and stained for 1-2 hours with primary  
738 antibody as indicated in 3% BSA, 0.05% saponin, PBS. Coverslips were washed 3 times 5  
739 min in 0.1% BSA, 0.05% saponin, PBS and incubated 1h with fluorochrome-conjugated  
740 secondary, washed 3 more times and embedded in Prolong Antifade Gold (Thermo Scientific).  
741 Stainings with Rab5 and Rab7 antibody (Cell Signalling) antibody were performed overnight  
742 in 3% BSA, 0.3% Tx-100, PBS at 4°C, followed by staining with additional primary antibody  
743 and secondary antibodies as above.

744

745 For Dil-LDL co-staining, cells were permeabilised for 40 sec in 0.01% Digitonin (Merck) and  
746 antibody stained in 3% BSA without detergent. For Filipin staining, cells were fixed and  
747 incubated 1 hour with 0.05mg/ml Filipin III (Cayman) in 0.5% BSA. For Filipin co-staining,  
748 primary and secondary antibody stainings were performed in the presence of Filipin and  
749 without detergent. Fluorescent staining was recorded on a Zeiss LSM880 Confocal  
750 microscope using a 63x oil objective and analysed using Zen v2.3 software (Zeiss).

751

752 For ORP1L/RILP-LAMP1 co-localisation, cells were transiently transfected with HA-tagged  
753 RILP or ORP1L constructs using Effectine (Qiagen), harvested at 24 hours post-transfection  
754 and fixed in 3.7% formaldehyde in PBS for 15-20 min. After 10min permeabilised with 0.1%  
755 TritonX-100 in PBS, coverslips were stained with HA and LAMP1 primary antibodies and  
756 donkey anti-rat CF568 and donkey anti-mouse Alexa647 secondary antibodies and mounted.  
757 Samples were imaged on a Leica SP8 microscope adapted with a HCX PL 63x 1.32 oil  
758 objective, solid-state lasers, and HyD detectors. Colocalisation was reported as Mander's  
759 coefficient calculated using JACoP plug-in for ImageJ on the basis of 2 independent  
760 experiments.

761

### 762 **LDL and EGF trafficking assays**

763 For LDL trafficking assays, cells were starved 30min in RPMI with 5% LPDS at 37°C, labelled  
764 15 min at 4°C with 20 µg/ml Dil-LDL in RPMI with 5% LPDS and 10mM HEPES, washed and  
765 chased for indicated times in full medium. For EGF trafficking, cells were starved for 1 hour in  
766 HBSS (Gibco), incubated with 100ng/ml EGF-AlexaFluor 555 for 5 min at 4°C, washed and  
767 chased in full medium. At indicated times, cells were fixed in 4% formaldehyde and either  
768 mounted directly or stained for indicated markers as described above. Fluorescent staining  
769 was recorded using a Zeiss LSM880 Confocal microscope with a 63x oil objective. EEA1+  
770 and LAMP1+ vesicles were annotated in an automated fashion using Volocity v6.3 software  
771 (Perkin-Elmer) and the percentage EGF within these vesicles was determined as a percentage  
772 of total EGF fluorescence for 5-6 fields per sample with >8 cells per field. To include luminal

773 content of enlarged LAMP1+ vesicles area filling function was enabled and enlarged vesicles  
774 were trimmed back by one pickle to prevent artificial area merging in areas of high vesicle  
775 density. Statistical significance was determined using two-tailed Student's T-Test with  
776 \*\* $p < 0.01$  and \*\*\* $p < 0.001$  and error bars reflecting standard error of mean (SEM).

777

#### 778 **Lysosomal cholesterol export assay**

779 Cells were seeded on coverslips and treated for 24 hours with 2  $\mu\text{M}$  U18666A (Santa Cruz) in  
780 RPMI with 10% FCS, washed with PBS and either fixed directly with 4% paraformaldehyde  
781 (pulse); or incubated for 24 hours in RPMI with 5% LPDS, 10 $\mu\text{M}$  mevastatin and 50 $\mu\text{M}$   
782 mevalonate (chase), then fixed. Coverslips were stained using Filipin and anti-CD63 antibody  
783 and analysed using a Zeiss LSM880 Confocal microscope with a 63x oil objective. Pearson's  
784 correlation between Filipin and CD63 staining was determined for three independent  
785 experiment using Volocity software (Perkin-Elmer) with 6 fields per sample and >8 cells per  
786 field. Statistical significance was determined using two-tailed Student's T-Test with \*\* $p < 0.01$   
787 and \*\*\* $p < 0.001$  and error bars reflecting standard error of mean (SEM).

788

#### 789 **Fluid phase endocytosis**

790 Bulk endocytosis and delivery of extracellular materials to the late endosomal compartment  
791 was measured using the dye Sulforhodamine 101 (SR101, Sigma), following published  
792 protocols<sup>44, 72</sup>. Briefly, Cells were seeded in live cell imaging dishes (MatTek), preincubated  
793 with LysoTracker Green (Molecular Probes) for 30 min, and SR101 dye was added directly to  
794 the cell medium at 25 $\mu\text{g}/\text{ml}$ . Samples were monitored by time-lapse on a Leica SP8  
795 microscope adapted with a climate control chamber using a HCX PL 63x 1.32 oil objective  
796 and images taken at multiple positions at 2 min intervals. SR101 colocalisation with the  
797 LysoTracker-positive compartment is reported as Mander's coefficient calculated using JACoP  
798 plug-in for ImageJ on the basis of 2 independent experiments. Total SR101 entering both cell  
799 lines was quantified at indicated time points by flow cytometry. Error bars indicate SD of the

800 mean. Statistical evaluations report on Student's T Test (analysis of two groups), with \*p<0.05,  
801 \*\*p<0.01, \*\*\*p<0.001.

802

### 803 **Electron microscopy**

804 Samples were prepared for cryo sectioning as follows <sup>73, 74</sup>. C18orf8-deficient cells and wild-  
805 type cells were fixed for either 2h in freshly prepared 2% paraformaldehyde and 0.2%  
806 glutaraldehyde in 0.1M phosphate buffer, or for 24h in freshly prepared 2% paraformaldehyde  
807 in 0.1 M phosphate buffer. Fixed cells were scraped, embedded in 12% gelatine (type A, bloom  
808 300, Sigma) and cut with a razor blade into 0.5 mm<sup>3</sup> cubes. The sample blocks were infiltrated  
809 in phosphate buffer containing 2.3 M sucrose. Sucrose-infiltrated sample blocks were  
810 mounted on aluminium pins and plunged in liquid nitrogen. The vitrified samples were stored  
811 under liquid nitrogen.

812

813 The frozen sample was mounted in a cryo-ultramicrotome (Leica). The sample was trimmed  
814 to yield a squared block with a front face of about 300 x 250 µm (Diatome trimming tool). Using  
815 a diamond knife (Diatome) and antistatic devise (Leica) a ribbon of 75 nm thick sections was  
816 produced that was retrieved from the cryo-chamber with the lift-up hinge method <sup>75</sup>. A droplet  
817 of 1.15 M sucrose was used for section retrieval. Obtained sections were transferred to a  
818 specimen grid previously coated with formvar and carbon.

819

820 Grids containing thawed cryo-sections of cells fixed with 2% paraformaldehyde and 0.2%  
821 glutaraldehyde were incubated on the surface of 2% gelatine at 37 °C. Subsequently grids  
822 were rinsed to remove the gelatine and sucrose and were embedded in 1.8% methylcellulose  
823 and 0.6% uranyl acetate. In case of additional gold-labelling, sections of cells fixed with 2%  
824 paraformaldehyde were incubated on drops with 1 µM TNM-BODIPY for 30 minutes on ice,  
825 washed, blocked with 1% BSA in PBS, and then incubated with rabbit polyclonal anti-BODPIY  
826 antibody <sup>47</sup>. Sections were subsequently labelled with 10 nm protein A-coated gold particles

827 (CMC, Utrecht University). EM imaging was performed with a Tecnai 20 transmission electron  
828 microscope (FEI) operated at 120 kV acceleration voltage.

829

830

### 831 **Identification of C18orf8 and NPC1 interaction partners by mass spectrometry (MS).**

832 HeLa cells, or HeLa cells expressing 3xHA-C18orf8, C18orf8-3xHA, GFP-3xHA or NPC1-  
833 3xHA were lysed in 1% Digitonin, HA-tagged proteins were immune precipitated for 2.5 hours  
834 at 4°C using Ezview anti-HA agarose (Sigma-Aldrich) as described above, eluted for 1h at  
835 37°C using 0.5 µg/ml HA peptide (Sigma-Aldrich) and denatured using 2% SDS, 50mM Tris  
836 pH7.4. Eluted samples were reduced with 10mM TCEP for 10mins RT and alkylated with  
837 40mM Iodoacetamide for 20mins RT in the dark. Reduced and alkylated samples were then  
838 submitted to digestion using the SP3 method (PMID: 25358341). Briefly, carboxylate coated  
839 paramagnetic beads are added to the sample and protein is bound to the beads by  
840 acidification with formic acid and addition of acetonitrile (ACN, final 50%). The beads are then  
841 washed sequentially with 100% ACN, 70% Ethanol (twice) and 100% ACN. 10uL of a buffer  
842 of TEAB (Triethylammonium bicarbonate) pH8 and 0.1% Sodium deoxycholate (SDC) is then  
843 added to the washed beads along with 100ng trypsin. Samples were then incubated overnight  
844 at 37 degrees with periodic shaking at 2000rpm. After digestion, peptides are immobilised on  
845 beads by addition of 200uL ACN and washed twice with 100uL ACN before eluting in 19uL  
846 2% DMSO and removing the eluted peptide from the beads.

847

### 848 **MS data acquisition**

849 Samples were acidified by addition of 1uL 10% TFA and the whole, 20uL sample injected.  
850 Data were acquired on an Orbitrap Fusion mass spectrometer (Thermo Scientific) running  
851 Xcalibur v4.3 (Thermo-Fisher) coupled to an Ultimate 3000 RSLC nano UHPLC (Thermo  
852 Scientific). Samples were loaded at 10 µl/min for 5 min on to an Acclaim PepMap C18 cartridge  
853 trap column (300 µm × 5 mm, 5 µm particle size) in 0.1% TFA. After loading a linear gradient  
854 of 3–32% solvent B over 60 or 90min was used for sample separation with a column of the

855 same stationary phase (75  $\mu\text{m}$   $\times$  75 cm, 2  $\mu\text{m}$  particle size) before washing at 90% B and re-  
856 equilibration. Solvents were A: 0.1% FA and B:ACN/0.1% FA. MS settings were as follows.  
857 MS1: Quadrupole isolation, 120'000 resolution, 5e5 AGC target, 50 ms maximum injection  
858 time, ions injected for all parallelisable time. MS2: Quadrupole isolation at an isolation width  
859 of m/z 0.7, HCD fragmentation (NCE 34) with the ion trap scanning out in rapid mode from,  
860 8e3 AGC target, 250 ms maximum injection time, ions accumulated for all parallelisable time.  
861 Target cycle time was 2s.

862

### 863 **MS data analysis**

864 Spectra were searched by Mascot v2.3 (Matrix Science) within Proteome Discoverer 2.1  
865 (Thermo-Fisher) in two rounds of searching. First search was against the UniProt Human  
866 reference proteome (26/09/17) and compendium of common contaminants (GPM). The  
867 second search took all unmatched spectra from the first search and searched against the  
868 human trEMBL database (UniProt, 26/0917). The following search parameters were used.  
869 MS1 Tol: 10 ppm, MS2 Tol: 0.6 Da, Fixed mods: Carbamindomethyl (C) Var mods: Oxidation  
870 (M), Enzyme: Trypsin (/P). PSM FDR was calculated using Mascot percolator and was  
871 controlled at 0.01% for 'high' confidence PSMs and 0.05% for 'medium' confidence PSMs.  
872 Proteins were quantified using the Minora feature detector within Proteome Discoverer and  
873 values normalised against the median protein abundance of the whole sample.

874

### 875 **Statistics and reproducibility**

876 The number of replicates of key experiments is indicated in the figure legends and/or methods  
877 section. Where not specifically indicated, experiments were performed once. All biological and  
878 biochemical experiments were performed with appropriate internal negative and/or positive  
879 controls as indicated. Most results were validated by different approaches and/or using  
880 alternative techniques as extensively reported in the manuscript. Confocal microscopy images

881 shown are representative of at least 5 fields, with co-localisation quantified as indicated in the  
882 figure legends and methods section.

883

## 884 **Data availability**

885 The authors declare that all data supporting the findings of this study are available within the  
886 paper and its supplementary information files. Source data are provided with this paper. The  
887 mass spectrometry proteomics data have been deposited to the ProteomeXchange  
888 Consortium via the PRIDE partner repository <sup>76</sup> with the dataset identifier PXD021444 and  
889 DOI 10.6019/PXD021444 [<http://dx.doi.org/10.6019/PXD021444>].

890

## 891 **Acknowledgments**

892 We are grateful to the following people for their help in this study: Dr. Michael Bassik (Stanford  
893 University) for kind donation of the genome-wide CRISPR/Cas9 sgRNA library and Prof. Ron  
894 Kopito and Dr. Matthew Porteus (Stanford University) for the pDonor CRISPR knock-in  
895 plasmid. FACS experiments were enabled by Dr. Reinard Schulte, Dr. Anna Petrunkina  
896 Harrison, the CIMR and JCBC FACS core facilities and confocal microscopy by Matthew  
897 Gratian and Mark Bowen. Stuart Bloor kindly assisted with Illumina sequencing, Dr. Ildar  
898 Gabaev with design of the top1000 CRISPR library, Dr. Peter Bailey with data analysis and  
899 Dr. James Williamson analyzed samples by mass spectrometry. Special thanks to Dr.  
900 Zhengzheng Sophia Liang (Harvard University) for fruitful discussions and moral support. This  
901 work was financially supported by a Wellcome Trust Principal Research Fellowship to P.J.L.  
902 (084957/Z/08/Z). J.P.L. was supported by MRC research grant MR/R0009015/1 and J.J.C.N. by  
903 ERC grant ERCOPE (GA 694307). The Cambridge Institute for Medical Research (CIMR) was  
904 in receipt of a Wellcome Trust strategic award (100140). The authors declare no competing  
905 financial interests.

906

## 907 **Author contributions**

908 DJHB and PJJ conceived the project. Experiments were carried out by DJHB, AS, IB, MLMJ  
909 and DME. DJHB analysed the data and prepared the figures. DJHB and PJJ wrote the  
910 manuscript. JJCN and JPL advised on the project and critically reviewed the manuscript.

911

## 912 **Conflict of interest**

913 The authors declare that they have no conflict of interest.

914

## 915 **Materials & Correspondence**

916 Correspondence and material requests should be addressed to PJJ ([pj30@cam.ac.uk](mailto:pj30@cam.ac.uk)) or  
917 DJHB ([djhv2@cam.ac.uk](mailto:djhv2@cam.ac.uk)).

918

919 **References:**

- 920 1. Brown, M.S. & Goldstein, J.L. The SREBP pathway: regulation of cholesterol metabolism by  
 921 proteolysis of a membrane-bound transcription factor. *Cell* **89**, 331-340 (1997).
- 922 2. Lund-Katz, S. & Phillips, M.C. Packing of cholesterol molecules in human low-density  
 923 lipoprotein. *Biochemistry* **25**, 1562-1568 (1986).
- 924 3. Goldstein, J.L. & Brown, M.S. The LDL receptor. *Arterioscler Thromb Vasc Biol* **29**, 431-438  
 925 (2009).
- 926 4. Pfeffer, S.R. NPC intracellular cholesterol transporter 1 (NPC1)-mediated cholesterol export  
 927 from lysosomes. *J Biol Chem* **294**, 1706-1709 (2019).
- 928 5. Watari, H. *et al.* Mutations in the leucine zipper motif and sterol-sensing domain inactivate  
 929 the Niemann-Pick C1 glycoprotein. *J Biol Chem* **274**, 21861-21866 (1999).
- 930 6. Li, X., Saha, P., Li, J., Blobel, G. & Pfeffer, S.R. Clues to the mechanism of cholesterol transfer  
 931 from the structure of NPC1 middle luminal domain bound to NPC2. *Proc Natl Acad Sci U S A*  
 932 **113**, 10079-10084 (2016).
- 933 7. Deffieu, M.S. & Pfeffer, S.R. Niemann-Pick type C 1 function requires luminal domain  
 934 residues that mediate cholesterol-dependent NPC2 binding. *Proc Natl Acad Sci U S A* **108**,  
 935 18932-18936 (2011).
- 936 8. Infante, R.E. *et al.* NPC2 facilitates bidirectional transfer of cholesterol between NPC1 and  
 937 lipid bilayers, a step in cholesterol egress from lysosomes. *Proc Natl Acad Sci U S A* **105**,  
 938 15287-15292 (2008).
- 939 9. Kwon, H.J. *et al.* Structure of N-terminal domain of NPC1 reveals distinct subdomains for  
 940 binding and transfer of cholesterol. *Cell* **137**, 1213-1224 (2009).
- 941 10. Pfeffer, S.R. Clues to NPC1-mediated cholesterol export from lysosomes. *Proc Natl Acad Sci*  
 942 *U S A* **113**, 7941-7943 (2016).
- 943 11. Luo, J., Jiang, L., Yang, H. & Song, B.L. Routes and mechanisms of post-endosomal cholesterol  
 944 trafficking: A story that never ends. *Traffic* **18**, 209-217 (2017).
- 945 12. Zhao, K. & Ridgway, N.D. Oxysterol-Binding Protein-Related Protein 1L Regulates Cholesterol  
 946 Egress from the Endo-Lysosomal System. *Cell Rep* **19**, 1807-1818 (2017).
- 947 13. Du, X. *et al.* A role for oxysterol-binding protein-related protein 5 in endosomal cholesterol  
 948 trafficking. *J Cell Biol* **192**, 121-135 (2011).
- 949 14. Chu, B.B. *et al.* Cholesterol transport through lysosome-peroxisome membrane contacts. *Cell*  
 950 **161**, 291-306 (2015).
- 951 15. Zhang, M. *et al.* MLN64 mediates mobilization of lysosomal cholesterol to steroidogenic  
 952 mitochondria. *J Biol Chem* **277**, 33300-33310 (2002).
- 953 16. Guerra, F. & Bucci, C. Multiple Roles of the Small GTPase Rab7. *Cells* **5** (2016).
- 954 17. Cantalupo, G., Alifano, P., Roberti, V., Bruni, C.B. & Bucci, C. Rab-interacting lysosomal  
 955 protein (RILP): the Rab7 effector required for transport to lysosomes. *EMBO J* **20**, 683-693  
 956 (2001).
- 957 18. Jordens, I. *et al.* The Rab7 effector protein RILP controls lysosomal transport by inducing the  
 958 recruitment of dynein-dynactin motors. *Curr Biol* **11**, 1680-1685 (2001).
- 959 19. Johansson, M., Lehto, M., Tanhuanpaa, K., Cover, T.L. & Olkkonen, V.M. The oxysterol-  
 960 binding protein homologue ORP1L interacts with Rab7 and alters functional properties of  
 961 late endocytic compartments. *Mol Biol Cell* **16**, 5480-5492 (2005).
- 962 20. Rocha, N. *et al.* Cholesterol sensor ORP1L contacts the ER protein VAP to control Rab7-RILP-  
 963 p150 Glued and late endosome positioning. *J Cell Biol* **185**, 1209-1225 (2009).
- 964 21. Sun, Q., Westphal, W., Wong, K.N., Tan, I. & Zhong, Q. Rubicon controls endosome  
 965 maturation as a Rab7 effector. *Proc Natl Acad Sci U S A* **107**, 19338-19343 (2010).
- 966 22. Liu, K. *et al.* WDR91 is a Rab7 effector required for neuronal development. *J Cell Biol* **216**,  
 967 3307-3321 (2017).

- 968 23. Rojas, R. *et al.* Regulation of retromer recruitment to endosomes by sequential action of  
969 Rab5 and Rab7. *J Cell Biol* **183**, 513-526 (2008).
- 970 24. Seaman, M.N., Harbour, M.E., Tattersall, D., Read, E. & Bright, N. Membrane recruitment of  
971 the cargo-selective retromer subcomplex is catalysed by the small GTPase Rab7 and  
972 inhibited by the Rab-GAP TBC1D5. *J Cell Sci* **122**, 2371-2382 (2009).
- 973 25. Zhang, X.M., Walsh, B., Mitchell, C.A. & Rowe, T. TBC domain family, member 15 is a novel  
974 mammalian Rab GTPase-activating protein with substrate preference for Rab7. *Biochem*  
975 *Biophys Res Commun* **335**, 154-161 (2005).
- 976 26. Frasa, M.A. *et al.* Armus is a Rac1 effector that inactivates Rab7 and regulates E-cadherin  
977 degradation. *Curr Biol* **20**, 198-208 (2010).
- 978 27. Cabrera, M. *et al.* The Mon1-Ccz1 GEF activates the Rab7 GTPase Ypt7 via a longin-fold-Rab  
979 interface and association with PI3P-positive membranes. *J Cell Sci* **127**, 1043-1051 (2014).
- 980 28. Nordmann, M. *et al.* The Mon1-Ccz1 complex is the GEF of the late endosomal Rab7  
981 homolog Ypt7. *Curr Biol* **20**, 1654-1659 (2010).
- 982 29. Lawrence, G. *et al.* Dynamic association of the PI3P-interacting Mon1-Ccz1 GEF with  
983 vacuoles is controlled through its phosphorylation by the type 1 casein kinase Yck3. *Mol Biol*  
984 *Cell* **25**, 1608-1619 (2014).
- 985 30. Wang, C.W., Stromhaug, P.E., Shima, J. & Klionsky, D.J. The Ccz1-Mon1 protein complex is  
986 required for the late step of multiple vacuole delivery pathways. *J Biol Chem* **277**, 47917-  
987 47927 (2002).
- 988 31. Kinchen, J.M. & Ravichandran, K.S. Identification of two evolutionarily conserved genes  
989 regulating processing of engulfed apoptotic cells. *Nature* **464**, 778-782 (2010).
- 990 32. Poteryaev, D., Datta, S., Ackema, K., Zerial, M. & Spang, A. Identification of the switch in  
991 early-to-late endosome transition. *Cell* **141**, 497-508 (2010).
- 992 33. Langemeyer, L., Perz, A., Kummel, D. & Ungermann, C. A guanine nucleotide exchange factor  
993 (GEF) limits Rab GTPase-driven membrane fusion. *J Biol Chem* **293**, 731-739 (2018).
- 994 34. Kiontke, S. *et al.* Architecture and mechanism of the late endosomal Rab7-like Ypt7 guanine  
995 nucleotide exchange factor complex Mon1-Ccz1. *Nat Commun* **8**, 14034 (2017).
- 996 35. Yasuda, S. *et al.* Mon1-Ccz1 activates Rab7 only on late endosomes and dissociates from the  
997 lysosome in mammalian cells. *J Cell Sci* **129**, 329-340 (2016).
- 998 36. Gerondopoulos, A., Langemeyer, L., Liang, J.R., Linford, A. & Barr, F.A. BLOC-3 mutated in  
999 Hermansky-Pudlak syndrome is a Rab32/38 guanine nucleotide exchange factor. *Curr Biol*  
1000 **22**, 2135-2139 (2012).
- 1001 37. Inoue, J., Sato, R. & Maeda, M. Multiple DNA elements for sterol regulatory element-binding  
1002 protein and NF-Y are responsible for sterol-regulated transcription of the genes for human 3-  
1003 hydroxy-3-methylglutaryl coenzyme A synthase and squalene synthase. *J Biochem* **123**,  
1004 1191-1198 (1998).
- 1005 38. Lam, A.J. *et al.* Improving FRET dynamic range with bright green and red fluorescent  
1006 proteins. *Nat Methods* **9**, 1005-1012 (2012).
- 1007 39. Morgens, D.W. *et al.* Genome-scale measurement of off-target activity using Cas9 toxicity in  
1008 high-throughput screens. *Nat Commun* **8**, 15178 (2017).
- 1009 40. Kelley, L.A., Mezulis, S., Yates, C.M., Wass, M.N. & Sternberg, M.J. The Phyre2 web portal for  
1010 protein modeling, prediction and analysis. *Nat Protoc* **10**, 845-858 (2015).
- 1011 41. Soding, J., Biegert, A. & Lupas, A.N. The HHpred interactive server for protein homology  
1012 detection and structure prediction. *Nucleic Acids Res* **33**, W244-248 (2005).
- 1013 42. Schroder, B. *et al.* Integral and associated lysosomal membrane proteins. *Traffic* **8**, 1676-  
1014 1686 (2007).
- 1015 43. Itzhak, D.N., Tyanova, S., Cox, J. & Borner, G.H. Global, quantitative and dynamic mapping of  
1016 protein subcellular localization. *Elife* **5** (2016).
- 1017 44. Wubbolts, R. *et al.* Direct vesicular transport of MHC class II molecules from lysosomal  
1018 structures to the cell surface. *J Cell Biol* **135**, 611-622 (1996).

- 1019 45. Maxfield, F.R. & Wustner, D. Analysis of cholesterol trafficking with fluorescent probes.  
1020 *Methods Cell Biol* **108**, 367-393 (2012).
- 1021 46. Nishimura, S. *et al.* Visualization of sterol-rich membrane domains with fluorescently-labeled  
1022 theonellamides. *PLoS One* **8**, e83716 (2013).
- 1023 47. Edgar, J.R., Manna, P.T., Nishimura, S., Banting, G. & Robinson, M.S. Tetherin is an exosomal  
1024 tether. *Elife* **5** (2016).
- 1025 48. Lu, F. *et al.* Identification of NPC1 as the target of U18666A, an inhibitor of lysosomal  
1026 cholesterol export and Ebola infection. *Elife* **4** (2015).
- 1027 49. Schultz, M.L. *et al.* Coordinate regulation of mutant NPC1 degradation by selective ER  
1028 autophagy and MARCH6-dependent ERAD. *Nat Commun* **9**, 3671 (2018).
- 1029 50. Gelsthorpe, M.E. *et al.* Niemann-Pick type C1 I1061T mutant encodes a functional protein  
1030 that is selected for endoplasmic reticulum-associated degradation due to protein misfolding.  
1031 *J Biol Chem* **283**, 8229-8236 (2008).
- 1032 51. Vanlandingham, P.A. & Ceresa, B.P. Rab7 regulates late endocytic trafficking downstream of  
1033 multivesicular body biogenesis and cargo sequestration. *J Biol Chem* **284**, 12110-12124  
1034 (2009).
- 1035 52. Shao, X. *et al.* Numb regulates vesicular docking for homotypic fusion of early endosomes via  
1036 membrane recruitment of Mon1b. *Cell Res* **26**, 593-612 (2016).
- 1037 53. Ao, X., Zou, L. & Wu, Y. Regulation of autophagy by the Rab GTPase network. *Cell Death*  
1038 *Differ* **21**, 348-358 (2014).
- 1039 54. Pontano Vaites, L., Paulo, J.A., Huttlin, E.L. & Harper, J.W. Systematic analysis of human cells  
1040 lacking ATG8 proteins uncovers roles for GABARAPs and the CCZ1/MON1 regulator  
1041 C18orf8/RMC1 in macro and selective autophagic flux. *Mol Cell Biol* (2017).
- 1042 55. Hirst, J. *et al.* Characterization of TSET, an ancient and widespread membrane trafficking  
1043 complex. *Elife* **3**, e02866 (2014).
- 1044 56. Jackson, L.P. *et al.* A large-scale conformational change couples membrane recruitment to  
1045 cargo binding in the AP2 clathrin adaptor complex. *Cell* **141**, 1220-1229 (2010).
- 1046 57. Dong, X.P. *et al.* PI(3,5)P(2) controls membrane trafficking by direct activation of mucolipin  
1047 Ca(2+) release channels in the endolysosome. *Nat Commun* **1**, 38 (2010).
- 1048 58. Raiborg, C. *et al.* Repeated ER-endosome contacts promote endosome translocation and  
1049 neurite outgrowth. *Nature* **520**, 234-238 (2015).
- 1050 59. Guillen-Samander, A., Bian, X. & De Camilli, P. PDZD8 mediates a Rab7-dependent  
1051 interaction of the ER with late endosomes and lysosomes. *Proc Natl Acad Sci U S A* (2019).
- 1052 60. Wong, Y.C., Ysselstein, D. & Krainc, D. Mitochondria-lysosome contacts regulate  
1053 mitochondrial fission via RAB7 GTP hydrolysis. *Nature* **554**, 382-386 (2018).
- 1054 61. Dong, J. *et al.* Allosteric enhancement of ORP1-mediated cholesterol transport by  
1055 PI(4,5)P2/PI(3,4)P2. *Nat Commun* **10**, 829 (2019).
- 1056 62. Wilhelm, L.P. *et al.* STARD3 mediates endoplasmic reticulum-to-endosome cholesterol  
1057 transport at membrane contact sites. *EMBO J* **36**, 1412-1433 (2017).
- 1058 63. Kumar, N. *et al.* VPS13A and VPS13C are lipid transport proteins differentially localized at ER  
1059 contact sites. *J Cell Biol* **217**, 3625-3639 (2018).
- 1060 64. Munoz-Braceras, S., Tornero-Ecija, A.R., Vincent, O. & Escalante, R. VPS13A is closely  
1061 associated with mitochondria and is required for efficient lysosomal degradation. *Dis Model*  
1062 *Mech* **12** (2019).
- 1063 65. Shammas, H., Kuech, E.M., Rizk, S., Das, A.M. & Naim, H.Y. Different Niemann-Pick C1  
1064 Genotypes Generate Protein Phenotypes that Vary in their Intracellular Processing,  
1065 Trafficking and Localization. *Sci Rep* **9**, 5292 (2019).
- 1066 66. Choudhury, A. *et al.* Rab proteins mediate Golgi transport of caveola-internalized  
1067 glycosphingolipids and correct lipid trafficking in Niemann-Pick C cells. *J Clin Invest* **109**,  
1068 1541-1550 (2002).

- 1069 67. Menzies, S.A. *et al.* The sterol-responsive RNF145 E3 ubiquitin ligase mediates the  
1070 degradation of HMG-CoA reductase together with gp78 and Hrd1. *Elife* **7** (2018).
- 1071 68. Doench, J.G. *et al.* Optimized sgRNA design to maximize activity and minimize off-target  
1072 effects of CRISPR-Cas9. *Nat Biotechnol* **34**, 184-191 (2016).
- 1073 69. Wang, T. *et al.* Identification and characterization of essential genes in the human genome.  
1074 *Science* **350**, 1096-1101 (2015).
- 1075 70. Langmead, B., Trapnell, C., Pop, M. & Salzberg, S.L. Ultrafast and memory-efficient alignment  
1076 of short DNA sequences to the human genome. *Genome Biol* **10**, R25 (2009).
- 1077 71. Li, W. *et al.* MAGeCK enables robust identification of essential genes from genome-scale  
1078 CRISPR/Cas9 knockout screens. *Genome Biol* **15**, 554 (2014).
- 1079 72. Jongsma, M.L. *et al.* An ER-Associated Pathway Defines Endosomal Architecture for  
1080 Controlled Cargo Transport. *Cell* **166**, 152-166 (2016).
- 1081 73. Peters, P.J., Bos, E. & Griekspoor, A. Cryo-immunogold electron microscopy. *Current*  
1082 *protocols in cell biology / editorial board, Juan S. Bonifacino ... [et al.] Chapter 4*, Unit 4 7  
1083 (2006).
- 1084 74. van Elsland, D.M. *et al.* Detection of bioorthogonal groups by correlative light and electron  
1085 microscopy allows imaging of degraded bacteria in phagocytes. *Chemical Science* **7**, 752-758  
1086 (2016).
- 1087 75. Bos, E. *et al.* A new approach to improve the quality of ultrathin cryo-sections; its use for  
1088 immunogold EM and correlative electron cryo-tomography. *J Struct Biol* **175**, 62-72 (2011).
- 1089 76. Perez-Riverol, Y. *et al.* The PRIDE database and related tools and resources in 2019:  
1090 improving support for quantification data. *Nucleic Acids Res* **47**, D442-D450 (2019).

1091

1092 **Figure legends**

1093

1094 **Fig. 1: A genome-wide CRISPR screen identifies essential factors in cellular cholesterol**

1095 **homeostasis. a-b** Creation of a HMGCS1-Clover CRISPR knock-in reporter in HeLa cells. **a**

1096 Schematic representation of the HMGCS1-Clover knock-in reporter and its induction upon

1097 sterol depletion by the SREBP2 transcription factor. **b** Immunoblotting of a reporter clone

1098 shows the endogenous HMGCS1-Clover fusion protein, detected by both HMGCS1- and

1099 GFP/Clover-specific antibody staining. **c-d** Sterol depletion induces HMGCS1-Clover

1100 expression in an SREBP-dependent manner. **c** HeLa HMGCS1-Clover cells were sterol

1101 depleted overnight and HMGCS1-Clover expression was analysed by microscopy.

1102 Representative images are shown from 5 fields per condition. Scale bars = 10 $\mu$ m. **d** HeLa

1103 HMGCS1-Clover CAS9 cells were transfected with sgRNA against *SREBF2* (red line) or

1104 control (blue and green lines), sterol depleted at day 7 (green and red lines) and HMGCS1-

1105 Clover expression was determined by flow cytometry. **e-g** Genome-wide CRISPR screening

1106 using the HMGCS1-Clover cholesterol reporter. **e** Schematic for the identification of genes

1107 essential for cellular cholesterol homeostasis. **f** HeLa HMGCS1-Clover/Cas9 cells were

1108 transduced with a genome-wide sgRNA library (220,000 sgRNAs). Rare HMGCS1- Clover<sup>high</sup>

1109 cells were isolated using two rounds of cell sorting, resulting in a 60% enriched HMGCS1-

1110 Clover<sup>high</sup> population (right panel, red line). **g** Illumina sequencing of sgRNAs in the isolated

1111 HMGCS1-Clover<sup>high</sup> population shows sgRNA enrichment for genes involved in cholesterol

1112 uptake (LDLR, NPC1, NPC2; blue), protein folding and glycosylation (yellow), membrane

1113 trafficking of LDLR/LDL (pink, purple, green) and SREBP2 function (orange). Genes with

1114 MAGeCK sgRNA enrichment score  $<10^{-5}$  are indicated by enrichment score and gene name.

1115 The full dataset is available in Supplementary Data 1.

1116

1117 **Fig. 2: A secondary sub-genomic CRISPR screen validates genes required for cellular**  
1118 **LDL-cholesterol uptake. a** Schematic of the primary (genome-wide) and secondary  
1119 (targeted, top 1000) screening approach. Screening results from both screens show extensive  
1120 overlap and create a complementary dataset of 106 genes required for cellular cholesterol  
1121 homeostasis. **b** Comparison of the genome-wide (vertical) and targeted (horizontal) CRISPR  
1122 screening results. Genes are indicated by MAGeCK sgRNA enrichment score, with hits  
1123 specific to the genome-wide screen (score  $<10^{-5}$ ) indicated in blue, hits specific to the targeted  
1124 screen (score  $<10^{-4}$ ) in green and hits in both screens in red. A select number of hits is  
1125 indicated by gene name. The full datasets are available in Supplementary Fig. 2 and  
1126 Supplementary Data 1. **c** A schematic representation of combined hits from the genome-wide  
1127 and targeted CRISPR screens highlights the central role of LDL-cholesterol import in cellular  
1128 cholesterol homeostasis. Hits are grouped by membrane trafficking pathway of their  
1129 involvement. A full list of hits from both screens is available in Supplementary Data 1.

1130

1131 **Fig. 3: C18orf8 is required for endosomal LDL-cholesterol uptake. a-b** *C18orf8*-deficient  
1132 cells show spontaneous cholesterol deficiency. **a** Wild-type and *C18orf8*-deficient clones were  
1133 lysed, endogenous *C18orf8* immunoprecipitated, and detected by a *C18orf8*-specific antibody.  
1134 **b** *C18orf8*-deficient HMGCS1-Clover clones were transduced with HA-tagged *C18orf8*  
1135 (*C18orf8*-3xHA; green lines) or empty vector (red lines) and HMGCS1-Clover expression was  
1136 determined by flow cytometry at day 18 using wild-type HMGCS1-Clover cells as a control  
1137 (black lines) (3 independent experimental replicates). **c** *C18orf8*-deficient cells are dependent  
1138 on endogenous cholesterol biosynthesis. Wild-type and *C18orf8*-deficient HMGCS1-Clover  
1139 cells were either cultured in LPDS to block exogenous LDL-cholesterol uptake (green lines),  
1140 treated with mevastatin to block endogenous cholesterol biosynthesis (red lines), or a  
1141 combination of both treatments (blue lines), after which cells were analysed by flow cytometry  
1142 for HMGCS1-Clover expression. **d-e** *C18orf8*-deficient cells show defective endo-lysosomal  
1143 LDL degradation. Wild-type, *C18orf8*-deficient or *C18orf8*-deficient cells complemented with

1144 C18orf8-3xHA were starved for 1 hour and pulse-labelled with fluorescent Dil-LDL, incubated  
1145 for 5 min (**d**) or 180 min (**e**), fixed and visualised by confocal microscopy. Exposure times were  
1146 kept constant between individual conditions at given time points. Representative images are  
1147 shown from 5 fields per condition. Scale bars = 10µm.

1148

1149 **Fig. 4: C18orf8-deficient cells show severe defects in late endosome morphology and**

1150 **early-to-late endosomal-trafficking. a-b** C18orf8-deficient cells show clustering of EE and

1151 swelling of LE/Ly. Confocal microscopy comparing EEA1 (blue), Rab7 (red) and LAMP1

1152 (green) in wild-type versus C18orf8-deficient cells. Representative images are shown from 5

1153 fields per condition and 2 independent experiments. **c-e** C18orf8-deficient cells have severe

1154 defects in early-to-late endosomal trafficking. **c-d** Wild-type and C18orf8-deficient cells were

1155 starved for 1 hour, pulse-labelled with AlexaFluor555-conjugated EGF (red), incubated for the

1156 indicated times, fixed and stained for EEA1 (blue) and LAMP1 (green). In **d** a cocktail of

1157 protease inhibitors (Leupeptin/E-64d/Pepstatin) was added during starve and chase to block

1158 EGF degradation. EEA1+ and LAMP1+ vesicles were identified using Volocity software and

1159 the percentage of EGF co-localising with these structures was determined from n=5 fields per

1160 condition with at least eight cells per field. Error bars reflect standard error of mean (two-sided

1161 unpaired t-test, \*\*\* p<0.001). **e** C18orf8-deficient cells were stimulated with Dil-LDL (red),

1162 chased for 3 hours, fixed and stained for EEA1 (blue) and LAMP1 (green). Representative

1163 images are shown from 5 fields. Scale bars = 10µm.

1164

1165 **Fig. 5: C18orf8 forms an integral component of the Mon1-Ccz1 (MC1) complex, essential**

1166 **for complex stability and function. a-c** C18orf8 interacts with the Mon1-Ccz1 complex.

1167 Immune precipitations of exogenous 3xHA-C18orf8 (N-term) or C18orf8-3xHA (C-term) were

1168 analysed by mass spectrometry (**a**) or Western blotting using Mon1B-, Ccz1- and HA-specific

1169 antibodies (**b**). Proteins detected by >3 peptides in both C18orf8 samples and absent from

1170 control, are indicated in **a**. Full MS results are available in Supplementary Data 2 and via  
1171 ProteomeXchange with identifier PXD021444 [<http://dx.doi.org/10.6019/PXD021444>]. **c**  
1172 Immune precipitation of an endogenous C18orf8-3xMyc fusion or Mon1B reveals a reciprocal  
1173 interaction between endogenous C18orf8, Ccz1 and Mon1B (see also Supplementary Fig.  
1174 5c). **d-e** C18orf8, Mon1B and Ccz1 show reciprocal stabilisation. Immunoblot analysis of  
1175 lysates from (**d**) wild-type, *C18orf8*-deficient and *C18orf8*-deficient cells complemented with  
1176 C18orf8-3xHA (3 independent experimental replicates); or (**e**) wild-type, *C18orf8*-, *Ccz1*- and  
1177 *Mon1A/B*-deficient cells. For endogenous C18orf8 detection, C18orf8 was immune  
1178 precipitated prior to immunoblotting (**e**). **f-g** *Ccz1*- and *Mon1A/B*-deficient cells show  
1179 cholesterol deficiency and disruption of LE/Ly morphology. **f** HMGCS1-Clover CAS9 cells  
1180 (black lines) were transfected with sgRNAs against *Mon1A*, *Mon1B*, *Mon1A* and *Mon1B*, *Ccz1*  
1181 or *Rab7* (red lines) or control (black lines), grown for 14 days, treated overnight with  
1182 mevastatin and analysed for HMGCS1-Clover expression. **g** Wild-type, *Ccz1*- and *Mon1A/B*-  
1183 deficient cells were stained intracellularly for EEA1 (blue), Rab7 (red) and LAMP1 (green).  
1184 Representative images are shown from 5 fields per condition. Scale bars = 10µm.

1185

1186 **Fig. 6: The trimeric Ccz1-Mon1-C18orf8 (MCC) complex activates mammalian Rab7. a**

1187 The MCC complex binds an inactive Rab7 (T22N). Immune precipitations of 2xHA-tagged  
1188 wild-type, T22N or Q67L Rab7 from *C18orf8*-3xMyc knock-in cells, were analysed by  
1189 immunoblot using Myc-, Ccz1- and Mon1B-specific antibodies (2 independent experimental  
1190 replicates, see also Supplementary Fig. 6a). **b-c** *C18orf8*-, *Ccz1*- and *Mon1A/B*-deficient cells  
1191 lack activation-dependent recruitment of Rab7 effectors. **b** Immune precipitations of 3xFLAG-  
1192 RILP from wild-type, *C18orf8*-, *Ccz1*- or *Mon1A/B*-deficient cells were analysed by  
1193 immunoblotting for endogenous Rab7 (2 independent experimental replicates). **c** Wild-type  
1194 and *C18orf8*-deficient cells were transfected with HA-RILP or ORP1L (Supplementary Fig. 7a)  
1195 and stained intracellularly for HA (green) and LAMP1 (magenta). Mander's correlation was  
1196 determined for n=5 fields per condition from 2 independent experiments. Error bars reflect

1197 standard deviation (two-sided unpaired t-test,  $p=2.1 \times 10^{-5}$ , \*\*\*  $p < 0.001$ ). **d-f** Cholesterol and  
1198 trafficking defects in *C18orf8*-deficient cells can be rescued by knockdown of Rab7GAPs or  
1199 expression of a constitutively active Rab7 (Q67L). **d** HMGCS1-Clover expression was  
1200 determined at day 8 after transduction with shRNAs against TBC1D5 (green), TBC1D15 (blue)  
1201 or both (red). **e-f** *C18orf8*-deficient cells were transduced with 2xHA-tagged Rab7-T22N  
1202 (green), -Q67L (red) or an empty vector (black) and either (**e**) analysed at day 10 by flow  
1203 cytometry for HMGCS1-Clover expression (2 independent experimental replicates, see also  
1204 Supplementary Fig 6b), or (**f**) pulse-labelled with Dil-LDL (red), incubated for 3 hours and  
1205 stained intracellularly for LAMP1 (green) and EEA1 (blue). Representative images are shown  
1206 from 5 fields per condition. Scale bars = 10 $\mu$ m.

1207

1208 **Fig. 7: *C18orf8*-, *Ccz1*- and *Mon1A/B*- (*MCC*)-deficient cells accumulate free cholesterol**  
1209 **in a swollen lysosomal compartment. a** Filipin staining of wild-type, *C18orf8*-deficient and  
1210 complemented *C18orf8*-deficient cells; or **c** wild-type, *Ccz1*- and *Mon1A/B*-deficient cells. **b**  
1211 Filipin (green) co-staining with the LE/Ly markers Rab7 (blue) and LAMP1 (red) in *C18orf8*-  
1212 deficient cells. **d** Theonellamides (TNM) immuno-gold labelling of wild-type and *C18orf8*-  
1213 deficient cells, visualised by EM. Multivesicular bodies (MVBs) are indicated by arrows. Note  
1214 MVBs are markedly enlarged in *C18orf8*-deficient cells. **e** Filipin staining of wild-type, *C18orf8*-  
1215 and *NPC1*-deficient cells. All confocal microscopy images are representative of 5 fields per  
1216 condition and 2 independent experiments. Scale bars for confocal microscopy = 10 $\mu$ m, scale  
1217 bars for EM = 200nm.

1218

1219 **Fig. 8: Rab7 interacts with the lysosomal cholesterol transporter NPC1 in an activation-**  
1220 **dependent manner. a** Immune-precipitation of HA-tagged NPC1 and detection of NPC1-  
1221 interacting proteins using mass spectrometry. Most abundant interaction partners detected  
1222 with >2 peptides are indicated (full dataset available in Supplementary Data 2 and via

1223 ProteomeXchange with identifier PXD021444 [<http://dx.doi.org/10.6019/PXD021444>]. **b**  
1224 Immune precipitations of HA-tagged wild-type, dominant-negative (T22N) or constitutively  
1225 active Rab7 (Q67L) show an activation-dependent interaction between Rab7 and endogenous  
1226 NPC1 (2 independent experimental replicates). **c-d** Reciprocal immune-precipitation of  
1227 endogenous NPC1 (**c**) or Rab7 (**d**) shows a strong interaction between both proteins. **e** The  
1228 Rab7-NPC1 interaction is lost in *MCC*-deficient cells that lack Rab7 activation. Wild-type,  
1229 *C18orf8*-, *Ccz1*- and *Mon1A/B*-deficient cells were stably transduced with the inactive NPC1-  
1230 P692S-HA. HA-tagged NPC1 was immune precipitated and immune blotted for endogenous  
1231 Rab7. The inactive NPC1-P692S was used to prevent altering lysosomal cholesterol content  
1232 by NPC1 overexpression. (2 independent experimental replicates) **f-g** The Rab7-NPC1  
1233 interaction is independent of NPC1 activity or lysosomal cholesterol levels. **f** *NPC1*-deficient  
1234 cells were complemented with HA-tagged wild-type or inactive P692S-mutant NPC1 and  
1235 NPC1-HA immune-precipitations were analysed by immune blotting for endogenous Rab7. **g**  
1236 Wild-type NPC1-HA complemented cells were treated with LPDS to decrease, or U18666A to  
1237 increase lysosomal cholesterol levels and the NPC1-Rab7 interaction was probed using  
1238 immune precipitation (2 independent experimental replicates).

1239

1240 **Fig. 9: Rab7 activation by the MCC GEF controls NPC1-dependent lysosomal**  
1241 **cholesterol export. a-d** Lysosomal cholesterol export is abolished in *NPC1*-, *C18orf8*-, *Ccz1*-  
1242 and *Mon1A/B*-deficient cells. **a** Schematic depiction of the cholesterol export assay. Similar to  
1243 a pulse-chase analysis, LDL-derived free cholesterol is allowed to accumulate in a lysosomal  
1244 compartment using the NPC1 inhibitor U18666A (pulse) and released during the LPDS chase.  
1245 **b** Free cholesterol (Filipin, green) accumulates in a CD63+ LE/Ly compartment (magenta) of  
1246 wild-type HeLa cells following 24h incubation with U18666A. **c** Wild-type, *NPC1*-, *C18orf8*-,  
1247 *Ccz1*- and *Mon1A/B*-deficient cells were treated for 24 hours with U18666A (top panels),  
1248 followed by a 24 hours chase in the presence of LPDS and mevastatin (lower panels).  
1249 Lysosomal cholesterol accumulation was visualised using Filipin (green) co-staining with the

1250 LE/Ly marker CD63 (magenta). **d** Co-localisation of Filipin with CD63 is plotted as Pearson  
1251 correlation, calculated from n=3 independent experiments with 6 fields per condition per  
1252 experiment and >8 cells per field. Error bars reflect standard error of mean (two-side paired t-  
1253 test, \*\* p<0.01, \*\*\* p<0.001). **e** Cholesterol accumulation in *C18orf8*-deficient cells is abolished  
1254 by overexpression of a hyperactive Rab7. *C18orf8*-deficient cells were transduced with a wild-  
1255 type, dominant-negative (T22N) or constitutively active Rab7 (Q67L) or empty vector and co-  
1256 stained with Filipin (green) and anti-CD63 (magenta). Representative images are shown from  
1257 5 fields per condition. **f** Rab7 overexpression rescues lysosomal cholesterol accumulation in  
1258 NPC patient fibroblasts. NPC1<sup>I1061T/I1061T</sup> primary patient fibroblasts were transduced with a  
1259 GFP-tagged wild-type Rab7 or vector control and analysed at day 7 for cholesterol  
1260 accumulation using Filipin staining. Fibroblasts from a healthy individual were used as a  
1261 control. Representative images are shown from 5 fields per condition and 2 independent  
1262 experiments (see also Supplementary Fig. 9). Scale bars = 10µm.

1263

1264 **Fig. 10: A trimeric Rab7 GEF controls NPC1-dependent lysosomal cholesterol export.**

1265 Model for MCC and Rab7 function in lysosomal cholesterol export. The trimeric Mon1-Ccz1-  
1266 C18orf8 (MCC) GEF activates mammalian Rab7, which binds the NPC1 cholesterol  
1267 transporter and either **a**) directly activates NPC1's cholesterol export function; or **b**) assembles  
1268 a down-stream membrane contact site (MCS) at which a yet-uncharacterised lipid transfer  
1269 protein (LTP) mediates cholesterol transfer to the ER and/or plasma membrane. A combined  
1270 Rab7 function in NPC1 activation and MCS formation would assure lysosomal cholesterol  
1271 export only proceeds once a down-stream lipid transfer module is assembled.

1272 **Supplementary methods.**

1273 Contains detailed information of DNA constructs, shRNA, sgRNA, DNA primers, gene  
1274 fragments and antibodies used within this study.

1275

1276 **Supplementary Data 1: Full datasets of the genome-wide and targeted HMGCS1-Clover**

1277 **CRISPR screens for cholesterol regulators.** Raw data from the primary (genome-wide) and  
1278 secondary (targeted, top 1000) HMGCS1-Clover CRISPR screens. Contains a full list of hits  
1279 from both screens, sgRNA read counts for library and enriched samples, screen analysis using  
1280 the MAGeCK algorithm and sgRNA sequences of the genome-wide Bassik and sub-genomic  
1281 top 1000 library.

1282

1283 **Supplementary Data 2: Full mass spectrometry dataset for C18orf8-3xHA and NPC1-**

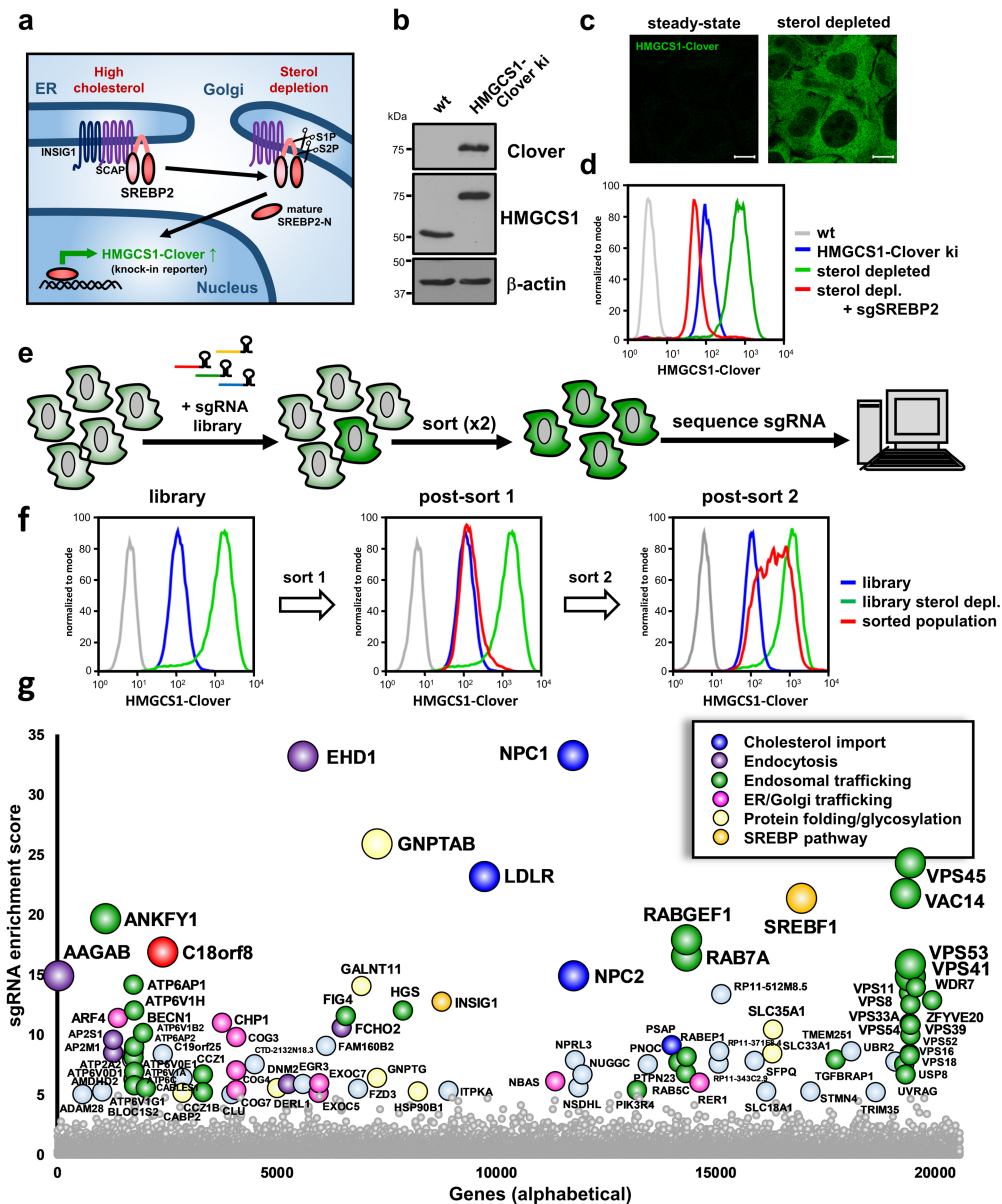
1284 **3xHA immune precipitations.** Proteins detected by  $\geq 2$  peptides and enriched  $>10$ -fold in  
1285 C18orf8-3xHA, 3xHA-C18orf8, or NPC1-3xHA immune precipitations versus control (GFP-  
1286 3xHA or vector) are indicated by gene name, number of peptides and summed peptide  
1287 abundance. Raw data are available via ProteomeXchange with identifier PXD021444  
1288 [<http://dx.doi.org/10.6019/PXD021444>].

1289

1290 **Source Data.**

1291 Contains uncropped versions of all Western blots and raw data underlying all reported  
1292 averages in graphs present within the manuscript.

1293



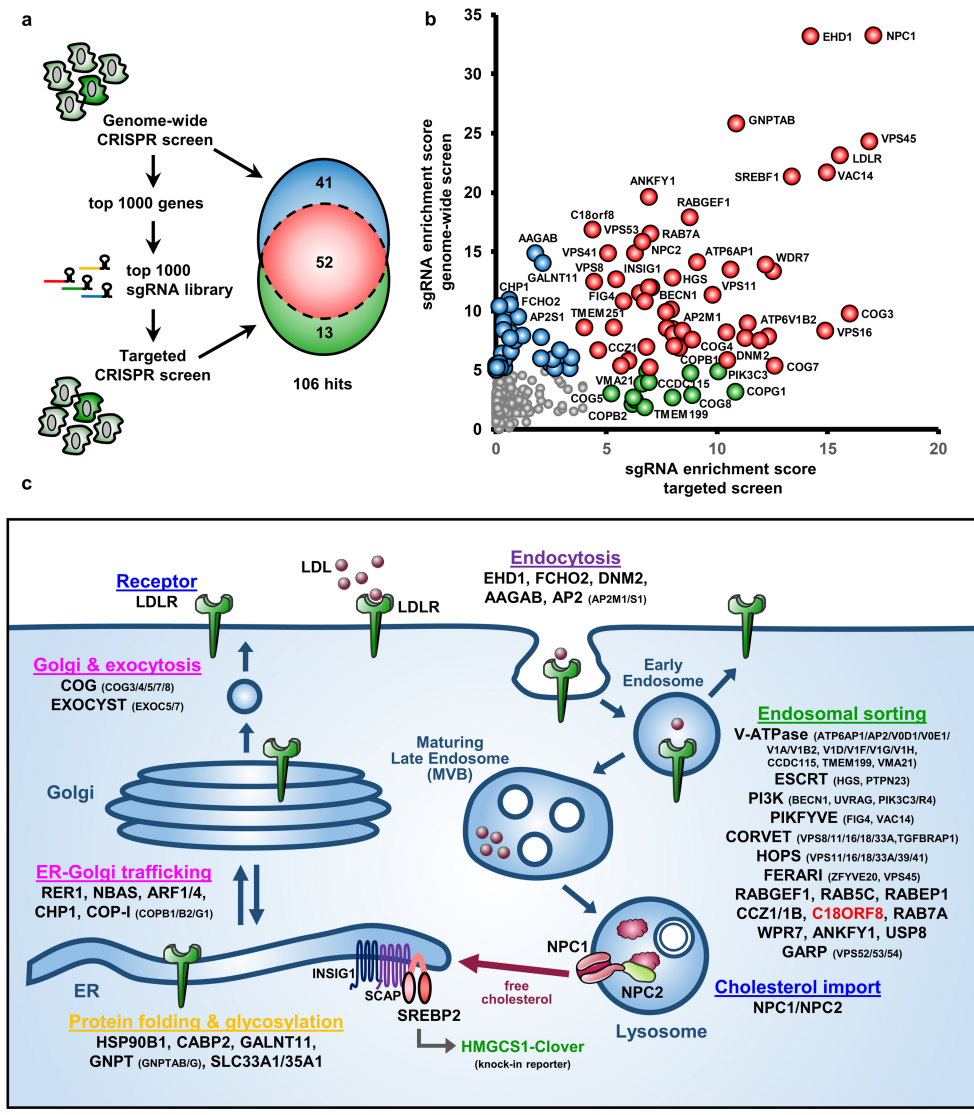
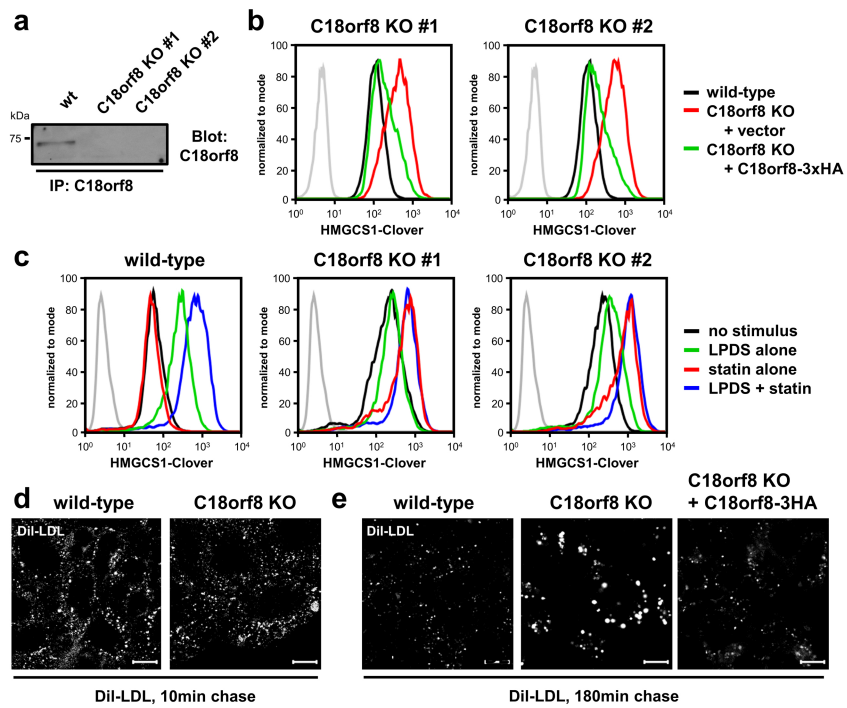
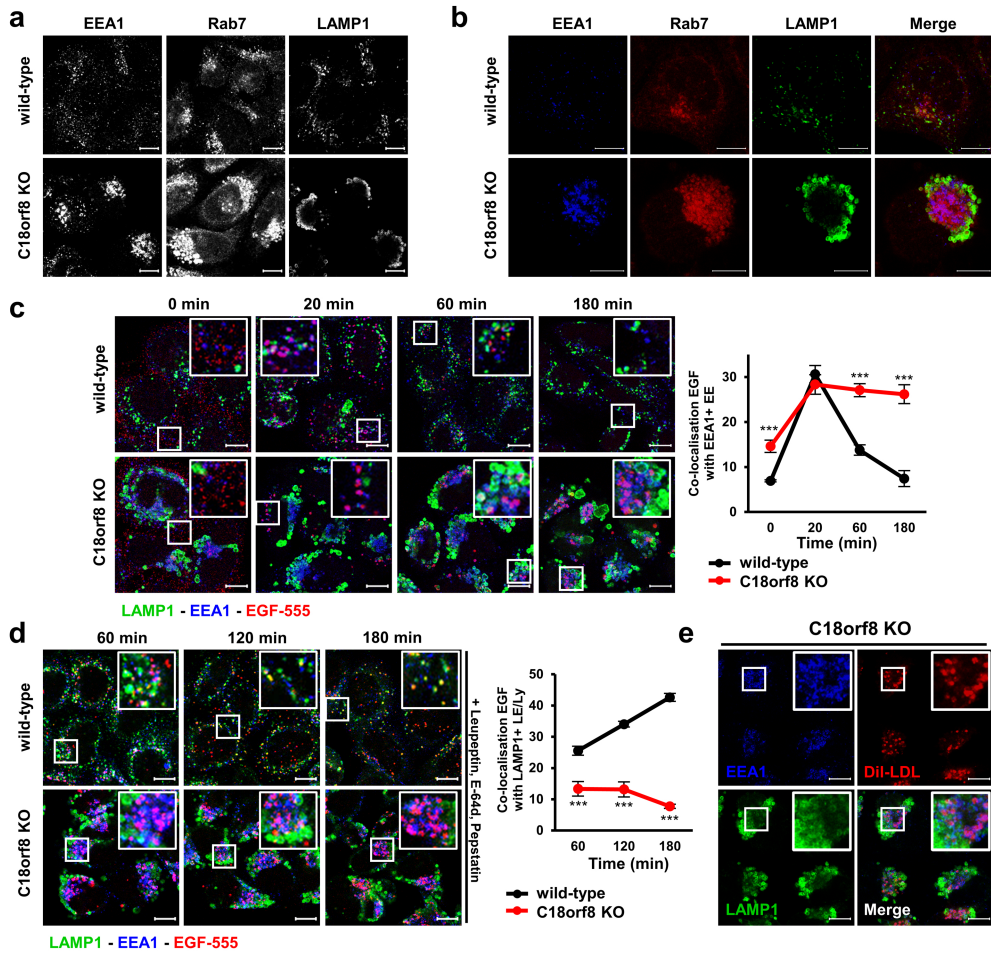


Fig. 2: A secondary sub-genomic CRISPR screen validates genes required for cellular LDL-cholesterol uptake



**Fig. 3: C18orf8 is required for endosomal LDL-cholesterol uptake**



**Fig. 4:** *C18orf8*-deficient cells show severe defects in late endosome morphology and early-to-late endosomal trafficking.

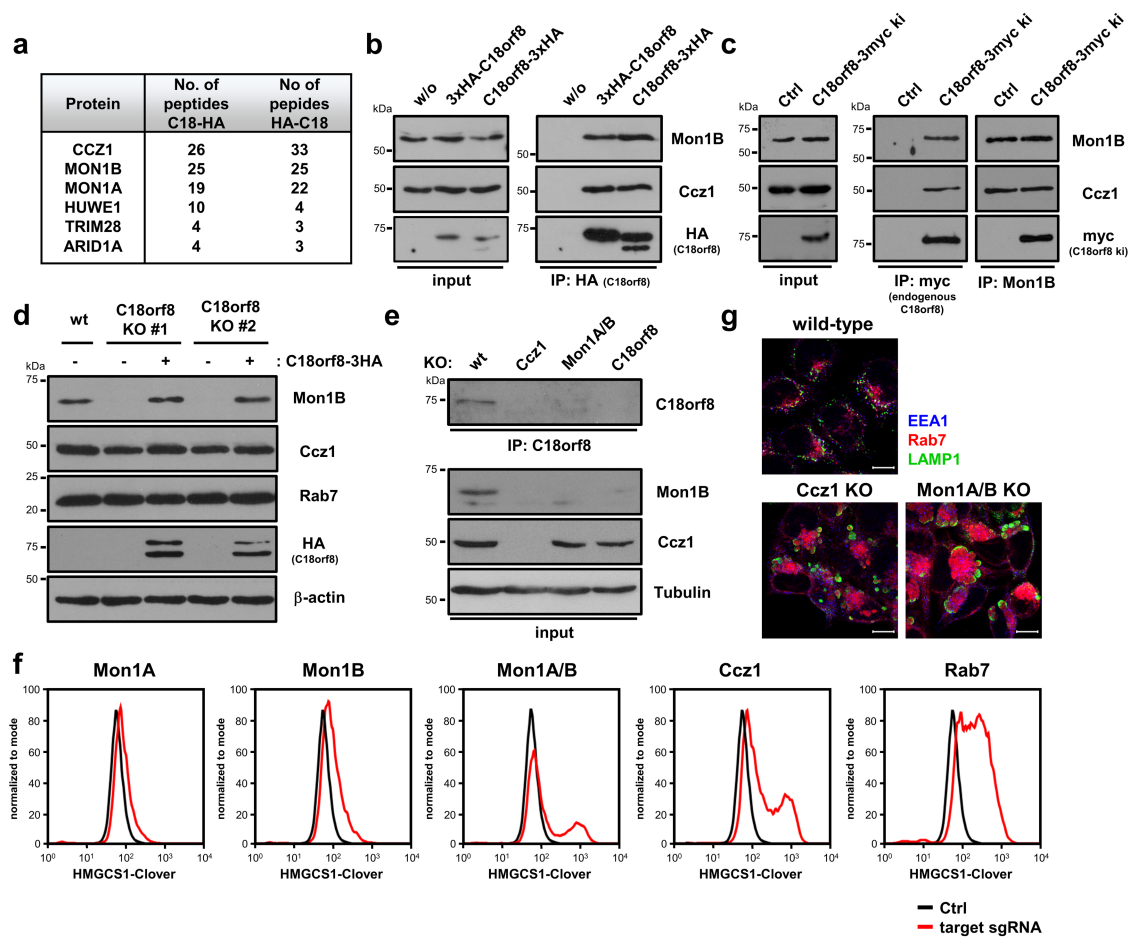


**Fig. 5: C18orf8 forms an integral component of the Mon1-Ccz1 (MC1) complex, essential for complex stability and function.**

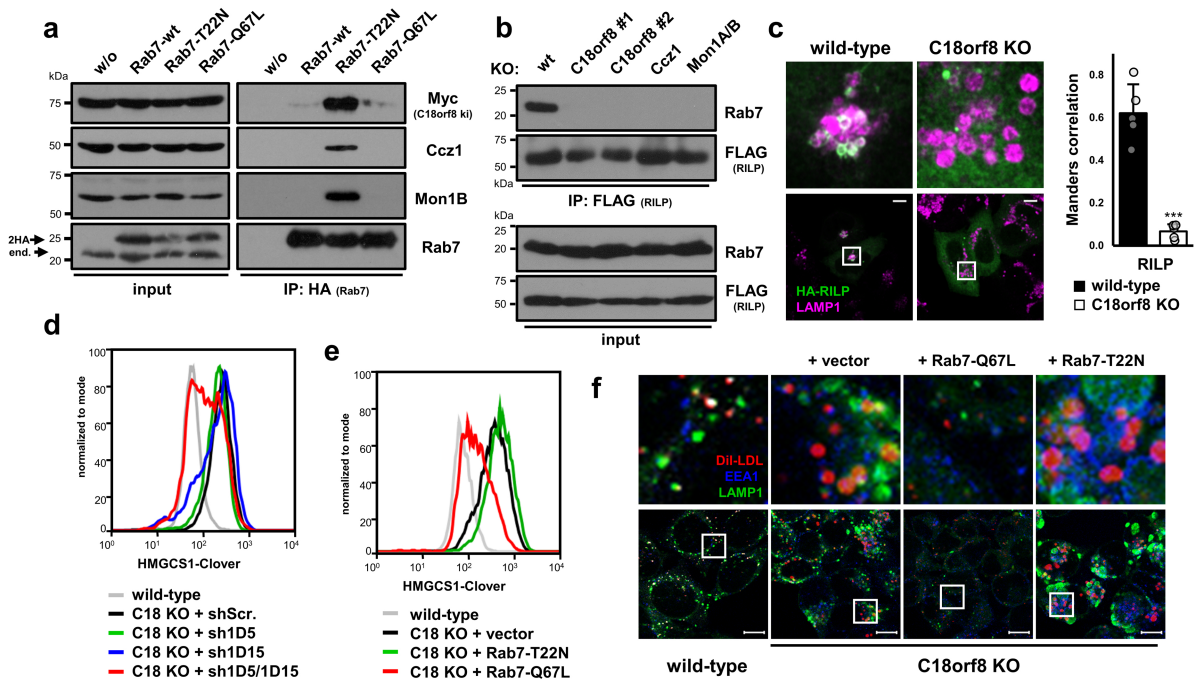


**Fig. 6: The trimeric Mon1-Ccz1-C18orf8 (MCC) complex activates mammalian Rab7.**

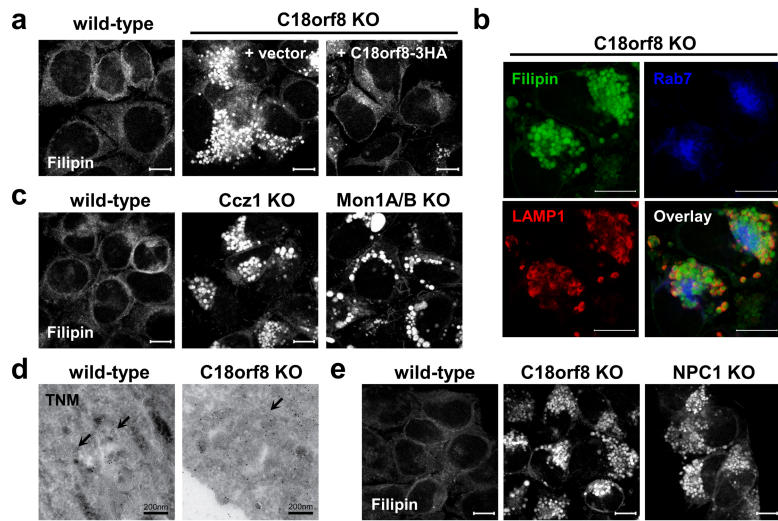
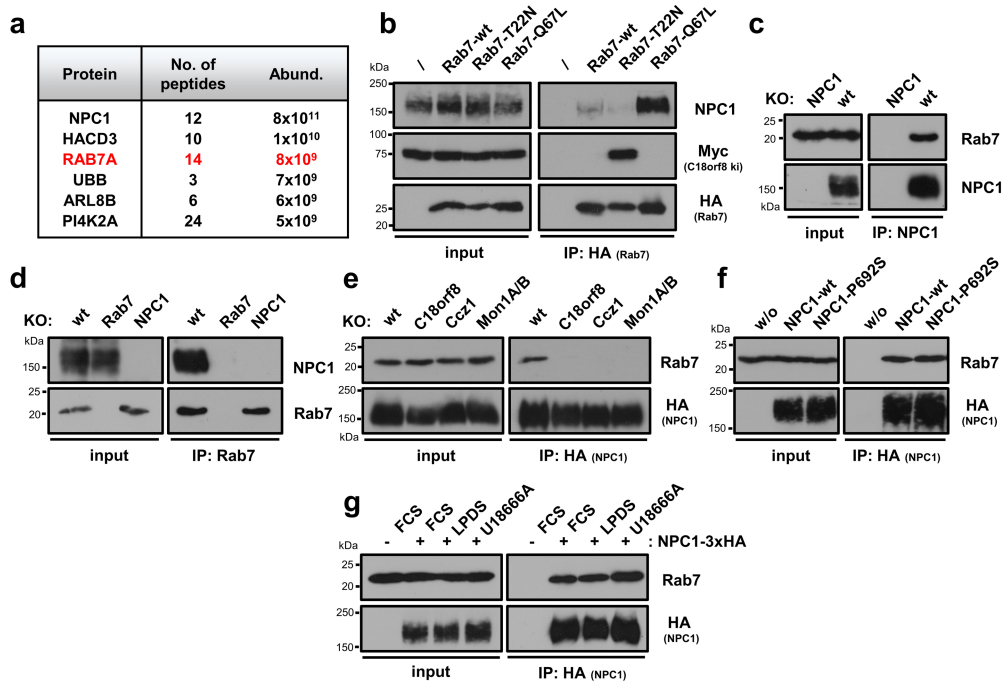


Fig. 7: *C18orf8*-, *Ccz1*- and *Mon1A/B*- (*MCC*)-deficient cells accumulate free cholesterol in a swollen lysosomal compartment.



**Fig. 8: Rab7 interacts with the lysosomal cholesterol transporter NPC1 in an activation-dependent manner.**

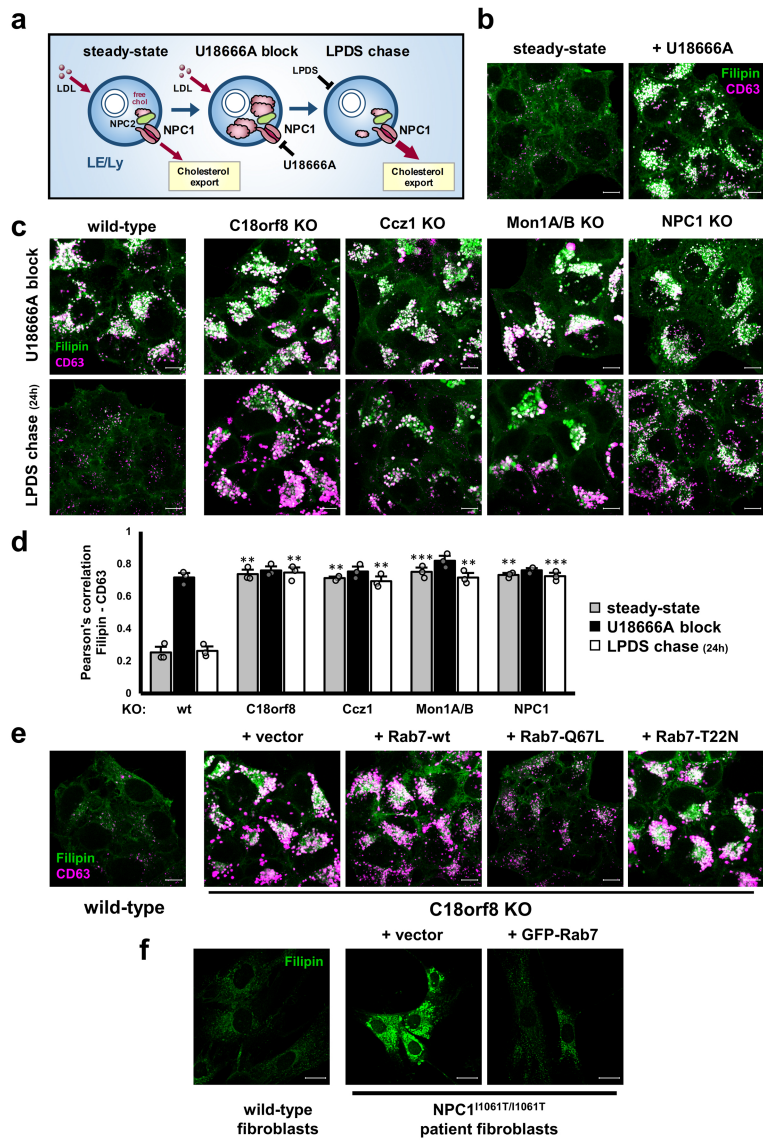
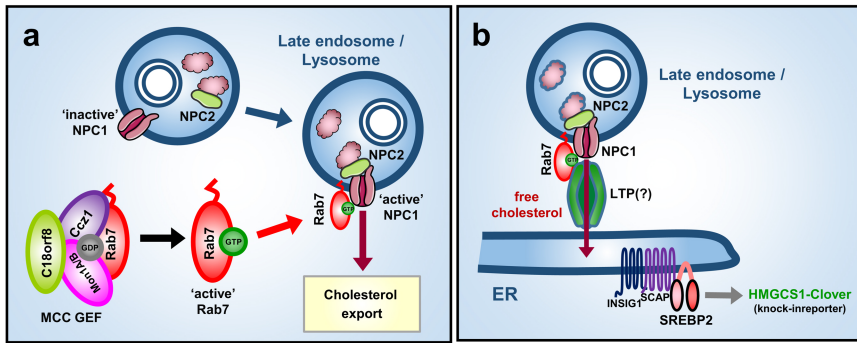


Fig. 9: Rab7 activation by the MCC GEF controls NPC1-dependent lysosomal cholesterol export.



**Fig. 10: A trimeric Rab7 GEF controls NPC1-dependent lysosomal cholesterol export.**